LEVEL II

12

NSWC/DL TR-3781

SHORT-CIRCUIT CURRENT FROM THE AXIAL-MODE SHOCK DEPOLING OF PZT 56/44 FERROELECTRIC CERAMIC DISKS

by
W. MOCK, Jr.
W. H. HOLT
Warheads Development Department

JANUARY 1978

NAVAL SURFACE WEAPONS CENTER
DAHLGREN LABORATORY
WHITE OAK LABORATORY
Dahlgren, Virginia 22448
Silver Spring, Maryland 20910

NAVAL SURFACE WEAPONS CENTER
Dahlgren, Virginia
22448

Paul J. Anderson, Capt., USN
Commander

UNCLASSIFIED

SECURITY CLASSIFICATION OF THIS PAGE (When Data Entered)

REPORT DOCUMENTATION PAGE

READ INSTRUCTIONS BEFORE COMPLETING FORM

1. REPORT NUMBER: TR-3781
2. GOVT ACCESSION NO.
3. RECIPIENT'S CATALOG NUMBER

4. TITLE (and Subtitle): SHORT-CIRCUIT CURRENT FROM THE AXIAL-MODE SHOCK DEPOLING OF PZT 56/44 FERROELECTRIC CERAMIC DISKS
5. TYPE OF REPORT & PERIOD COVERED: Final
6. PERFORMING ORG. REPORT NUMBER

7. AUTHOR(s): W. Mock, Jr.; W. H. Holt
8. CONTRACT OR GRANT NUMBER(s)

9. PERFORMING ORGANIZATION NAME AND ADDRESS: Naval Surface Weapons Center (G30), Dahlgren, Virginia 22448
10. PROGRAM ELEMENT, PROJECT, TASK AREA & WORK UNIT NUMBERS: 62332N/F00382/ WF00382501

11. CONTROLLING OFFICE NAME AND ADDRESS: Naval Air Systems Command, Washington, DC 20360
12. REPORT DATE: Jan[redacted] 1978
13. NUMBER OF PAGES: 73

14. MONITORING AGENCY NAME & ADDRESS (if different from Controlling Office)
15. SECURITY CLASS. (of this report): UNCLASSIFIED
15a. DECLASSIFICATION/DOWNGRADING SCHEDULE

16. DISTRIBUTION STATEMENT (of this Report)

Approved for public release; distribution unlimited.

17. DISTRIBUTION STATEMENT (of the abstract entered in Block 20, if different from Report)

18. SUPPLEMENTARY NOTES

19. KEY WORDS (Continue on reverse side if necessary and identify by block number)

Ferroelectric Ceramics
Shock Waves
Gas Gun
Shock-Depoled Ferroelectrics
Electrical Breakdown
Polarization Reversal
Electrical Depoling Path

20. ABSTRACT (Continue on reverse side if necessary and identify by block number)

Gas gun impact techniques have been used to investigate the electrical response of shock-depoled PZT 56/44 ferroelectric ceramic disks in the stress range from 0.7 to 8.8 GPa. External short-circuit current pulses were measured as the shock wave propagated axially through the disk in a direction either parallel or antiparallel to the remanent polarization vector. Complete charge release was not observed in any of the shots. About 82% of the available charge was released for both orientations in the stress range from 1.5 to 5.6 GPa. At stress levels of 6.8 and 8.8 GPa, the charge release for

(Cont'd on back)

DD FORM 1 JAN 73 1473 EDITION OF 1 NOV 65 IS OBSOLETE S/N 0102-LF-014-6601

UNCLASSIFIED

SECURITY CLASSIFICATION OF THIS PAGE (When Data Entered)

(20)

the antiparallel orientation shots was less than for the parallel orientation shots. A series of electrical polarization reversal measurements was performed under nonshock conditions on PZT disks to estimate the electrical properties in the region ahead of the shock front. Maximum electric fields for the regions ahead of and behind the shock front were estimated to be 1 to 6 kV/mm and 4 to 24 kV/mm, respectively, as the shock stress was increased.

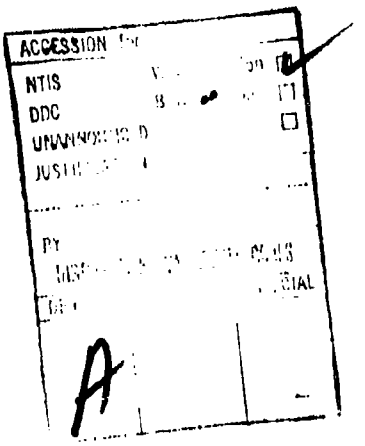

FOREWORD

The electrical properties of PZT 56/44 ferroelectric ceramic disks have been investigated under shock wave compression in axial-current-mode experiments. These properties are important for applications involving single-shot ferroelectric pulse power supplies. Funding for this work was provided by NAVAIR Task No. A310310B/009A/4R02103002.

This report has been reviewed by C. A. Cooper, Head, Munitions Division.

Released by:

CDR JAMES R. WILLIAMS
Assistant Head for Military Applications
Armaments Development Department

ACKNOWLEDGMENTS

The authors would like to thank E. J. Shuler for designing, fabricating, and performing the circuit analysis calculations for the electrical circuit used in the high-frequency polarization reversal measurements. The authors would also like to thank P. C. Lysne of Sandia Laboratories for helpful discussions.

TABLE OF CONTENTS

	Page
FOREWORD	iii
ACKNOWLEDGEMENTS	iv
LIST OF ILLUSTRATIONS	vi
LIST OF TABLES	viii
I. INTRODUCTION	1
II. PZT MATERIAL	3
III. LOW- AND HIGH-FREQUENCY ELECTRICAL POLARIZATION REVERSAL MEASUREMENTS	4
IV. EXPERIMENTAL TECHNIQUE FOR SHOCK-DEPOLING MEASUREMENTS	13
V. RESULTS AND DISCUSSION	17
VI. SUMMARY	43
REFERENCES	44
APPENDIXES	
A – OSCILLOSCOPE RECORDS FOR POLARIZATION REVERSAL EXPERIMENTS	A-1
B – OSCILLOSCOPE RECORDS FOR SHOCK-DEPOLING EXPERIMENTS	B-1
DISTRIBUTION	

LIST OF ILLUSTRATIONS

Figure		Page
1	Schematic of axial-current-mode shock-depoling experiment.	2
2	Schematic of Sawyer-Tower circuit for measuring a low-frequency hysteresis loop for a ferroelectric disk (Reference 8).	4
3	Oscilloscope record of low-frequency hysteresis loop for a PZT 56/44 disk.	5
4	Schematic of circuit for performing polarization reversal measurements on PZT disks under high-field and high-frequency conditions.	6
5	Voltage and current records for pulse charging a 2.2-nF nonferroelectric ceramic capacitor.	7
6	Voltage and current records for pulse charging a PZT 56/44 disk for a source capacitor voltage of 7 kV.	8
7	Polarization-reversal electric field curves for PZT 56/44 disks as a function of increasing source capacitor voltage.	10
8	Polarization-reversal current pulses for PZT 56/44 disks as a function of increasing source capacitor voltage.	11
9	Changes in electric displacement versus electric field for PZT 56/44 disks.	13
10	Schematic of muzzle region of gas gun showing the details of the target assembly for the axial-current-mode depoling of a PZT disk.	14
11	PZT target assembly on granite surface plate before epoxy pour.	16
12	PZT target assembly on gas gun muzzle prior to firing gun.	18
13	Peak current versus shock stress for PZT 56/44 disks.	23
14	Time of peak current versus shock stress for PZT 56/44 disks.	24
15	Charge release versus shock stress for PZT 56/44 disks.	26
16	Current pulses for the antiparallel and parallel orientation shots at a shock stress of 0.7 GPa.	27
17	Current pulses for the antiparallel and parallel orientation shots at a shock stress of 1.5 GPa.	27
18	Current pulses for the antiparallel and parallel orientation shots at a shock stress of 2.2 GPa.	28

LIST OF ILLUSTRATIONS (Continued)

Figure		Page
19	Current pulses for the 2.7-GPa antiparallel orientation shot and 2.6-GPa parallel orientation shot.	28
20	Current pulses for the antiparallel and parallel orientation shots at a shock stress of 3.3 GPa.	29
21	Current pulses for the antiparallel and parallel orientation shots at a shock stress of 3.9 GPa.	29
22	Current pulses for the antiparallel and parallel orientation shots at a shock stress of 4.7 GPa.	30
23	Current pulses for the 5.6-GPa antiparallel orientation shot and the 5.5-GPa parallel orientation shot.	30
24	Current pulses for the antiparallel and parallel orientation shots at a shock stress of 6.8 GPa.	31
25	Current pulses for the 8.6-GPa antiparallel orientation shot and the 8.8-GPa parallel orientation shot.	31
26	Current pulses for the antiparallel orientation shots.	33
27	Current pulses for the parallel orientation shots.	33
28	Charge release versus shock stress curves for the axial-current-mode depoling of PZT 56/44, PZT 95/5, and PSZT 68/7 ferroelectric ceramic disks.	35
29	Schematic for the axial-current-mode depoling of a PZT disk in the antiparallel and parallel orientations.	37
30	A plot of the current pulse i, the electric fields E_1 and E_2 in the shocked and unshocked regions, respectively, and the electric displacement D in the PZT specimen for the 2.2-GPa antiparallel orientation shot.	40
31	A plot of the current pulse i, the electric fields E_1 and E_2 in the shocked and unshocked regions, respectively, and the electric displacement D in the PZT specimen for the 6.8-GPa parallel orientation shot.	40
32	Estimated initial dielectric constant in the shocked region versus shock stress.	42
A-1	Polarization-reversal voltage and current records for a PZT disk for a source capacitor voltage of 2 kV.	A-3
A-2	Polarization-reversal voltage and current records for a PZT disk for a source capacitor voltage of 3 kV.	A-3
A-3	Polarization-reversal voltage and current records for a PZT disk for a source capacitor voltage of 4 kV.	A-4

LIST OF ILLUSTRATIONS (Continued)

Figure		Page
A-4	Polarization-reversal voltage and current records for a PZT disk for a source capacitor voltage of 6 kV.	A-4
A-5	Polarization-reversal voltage and current records for a PZT disk for a source capacitor voltage of 7 kV.	A-5
B-1	Current records for (a) Shot 38 and (b) Shot 39.	B-3
B-2	Current records for (a) Shot 42 and (b) Shot 41.	B-3
B-3	Current records for (a) Shot 36 and (b) Shot 37.	B-4
B-4	Current records for (a) Shot 49 and (b) Shot 45.	B-4
B-5	Current records for (a) Shot 44 and (b) Shot 46.	B-5
B-6	Current records for (a) Shot 48 and (b) Shot 47.	B-5
B-7	Current records for (a) Shot 50 and (b) Shot 51.	B-6
B-8	Current records for (a) Shot 54 and (b) Shot 55.	B-6
B-9	Current records for (a) Shot 52 and (b) Shot 56.	B-7
B-10	Current records for (a) Shot 53 and (b) Shot 57.	B-7

LIST OF TABLES

Table		Page
1	Average piezoelectric and ferroelectric properties of PZT 56/44 disks.	3
2	Results of polarization reversal experiments.	9
3	Impactor and specimen parameters for shock-depoling experiments.	19
4	Results of shock-depoling experiments.	20
5	Results of ultrasonic velocity measurements.	34

I. INTRODUCTION

In recent years, poled lead zirconate titanate (PZT) ferroelectric ceramics have found wide application as reversible generators of electromechanical energy because of their superior piezoelectric properties. Examples of piezoelectric PZT devices include accelerometers, ultrasonic cleaning transducers, underwater detection devices, and gasoline motor ignition devices.[1] In these applications, a device operates in the linear piezoelectric range of the material; that is, the induced electric fields and stresses are not large enough to destroy its piezoelectric properties.

Another application of PZT ferroelectric ceramics is their use as elements in shock-excited pulse power supplies.[2] For these devices the linear piezoelectric limit of the material is far exceeded. As the shock wave passes through the ceramic and alters the polarized state, the bound surface charge which is held in position on the PZT electrodes is released. Because this charge release is a complicated function of the stress state, to properly design pulse power supplies it is necessary to understand the electrical response of PZT ceramics under shock wave compression.[2,3]

We present in this report the results of an investigation of the axial-current-mode response of shock-depoled PZT 56/44 ferroelectric ceramic disks in the stress range from 0.7 to 8.8 GPa. (PZT 56/44 is a solid solution containing 56 mole % lead zirconate and 44 mole % lead titanate with niobium, strontium, and lanthanum as minor added constituents.) Figure 1 is a schematic of the experimental arrangement. The PZT remanent polarization vector is parallel to the axis of the disk. On impact, a shock wave is generated at the projectile-PZT interface. The magnitude and shape of the external short circuit current pulse and the charge release are used to investigate the electrical properties of the shock-depoled PZT disk.

Experiments were performed for the specimen remanent polarization vector oriented both parallel and antiparallel to the shock wave propagation direction in order to compare the current pulses and charge release for the two orientations. Cutchen[4] found that the voltage pulses for the axial-voltage-mode depoling of PZT 65/35 disks showed an orientational dependence. (PZT 65/35 is a solid solution containing 65 mole % lead zirconate and 35 mole % lead titanate with niobium as a minor added constituent.) For that material electrical breakdown and conduction were more pronounced for the antiparallel orientation than for the parallel orientation. An orientational dependence has also been reported by Graham and Halpin.[5]

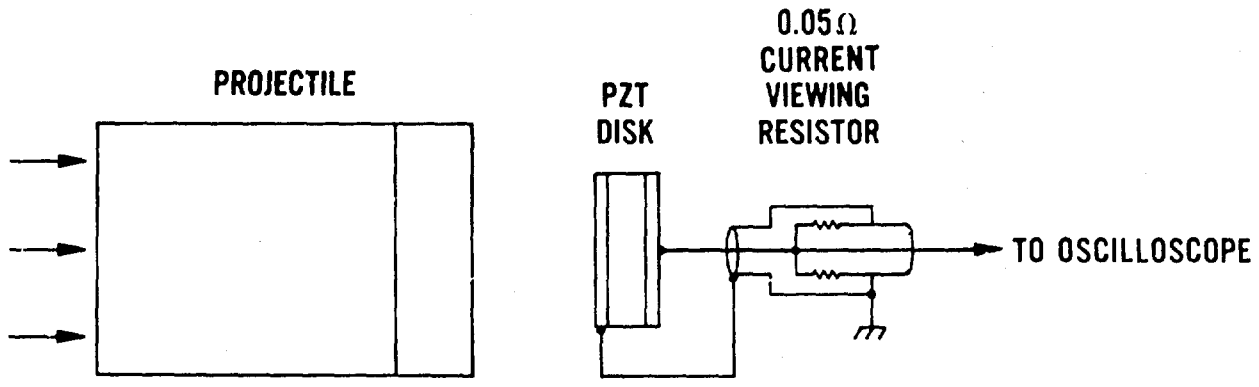

Figure 1. Schematic of axial-current-mode shock-depoling experiment.

In addition to the shock-depoling experiments, a series of low- and high-frequency electrical polarization reversal measurements was performed on PZT 56/44 disks. The low-frequency depoling path was obtained for comparison with the high-frequency depoling path data. The high-frequency measurements were obtained to estimate the electrical depoling path for the region ahead of the shock front in the shock-depoling experiments. In PZT 95/5 axial-current-mode experiments, Halpin[3,6] estimated the high-frequency coercive field by using the low-frequency electrical depoling path in curve fits to the experimental current-time data. (PZT 95/5 is a solid solution containing 95 mole % lead zirconate and 5 mole % lead titanate with niobium as a minor added constituent.)

In Section II, the piezoelectric and ferroelectric properties are presented for the PZT 56/44 ceramic disks used in this investigation. Section III contains the results of the low- and high-frequency polarization reversal measurements for the PZT disks. A discussion of the experimental techniques and target assembly preparation procedure for the shock wave experiments is presented in Section IV. The experimental results for the shock-depoling experiments are presented and discussed in Section V. Section VI is the summary. Appendix A contains the voltage and current oscilloscope records for the high-frequency polarization reversal measurements. Appendix B contains the current oscilloscope records for the shock-depoling experiments.

II. PZT MATERIAL

The PZT 56/44 ferroelectric ceramic disks used in this investigation were purchased from Gulton Industries, Inc. The disks were normal fired. They had a thickness of 0.76 mm and a diameter of 14 mm. A disk had 12.7-mm-diameter fired-on silver electrodes located in the center of the disk and a 0.64-mm-wide nonelectroded region located at the edge of the disk. The average electrode thickness was 8 μm (average for 15 specimens). The average density for eight specimens (electrodes removed) was 7.50 Mg/m^3. This composition has rhombohedral structure[7] and is located near the rhombohedral-tetragonal phase boundary of the $PbZrO_3$ and $PbTiO_3$ phase diagram.[1]

Table 1 lists some of the piezoelectric and ferroelectric properties of the PZT disks. K_3 is the low-frequency dielectric constant in the polarization direction. The piezoelectric voltage and charge coefficients are, respectively, the ratios of the electric field and generated charge to the stress applied in the polarization direction. They are related through the equation $d_{33} = K_3 \epsilon_0 g_{33}$ where ϵ_0 is the permittivity of free space. The planar coupling coefficient k_p describes the conversion of mechanical energy to electrical energy and vice versa for a thin disk vibrating in radial expansion and contraction. These coefficients are useful only for stresses that are a small fraction of a gigapascal.[7] For larger stresses, permanent depoling occurs, and the piezoelectric properties of the material are degraded. The last two columns in the table give the parameters that characterize the ferroelectricity of the material. The remanent polarization P_0 and the coercive field E_c were obtained for a 60-sec hysteresis loop. E_c is the electric field required to reduce the material polarization to zero.

Table 1. Average piezoelectric and ferroelectric properties of PZT 56/44 disks.[a]

Dielectric Constant K_3	Piezoelectric Voltage Coefficient g_{33} (V · m/N)	Piezoelectric Charge Coefficient d_{33} (pC/N)	Planar Coupling Coefficient k_p	Remanent Polarization P_0 ($\mu C/mm^2$)	Low-Frequency Coercive Field E_c (kV/mm)
2480	18×10^{-3}	400	0.604	0.31	1.0

[a]This data was provided by Gulton Industries, Inc., Fullerton, CA, and is the average of measurements for four disks.

III. LOW- AND HIGH-FREQUENCY ELECTRICAL POLARIZATION REVERSAL MEASUREMENTS

The low-frequency measurements consisted of obtaining 60-Hz hysteresis loops for the PZT 56/44 disks. A schematic of the Sawyer-Tower circuit[8] that was fabricated for the measurements is shown in Figure 2. The technique consists of measuring the voltage and associated stored charge on the PZT specimen. The voltage across the 2.24-μF integrating capacitor measures the charge on the specimen disk and is displayed on the vertical axis of oscilloscope. The voltage on the specimen is measured with a voltage probe (Tektronix P6015, 40 kV peak, 1000X attenuation) and is displayed on the horizontal axis of oscilloscope. The specimen disk is placed between two 12.7-mm-diameter brass electrodes and immersed in transformer oil to reduce the possibility of electrical breakdown along its edges.

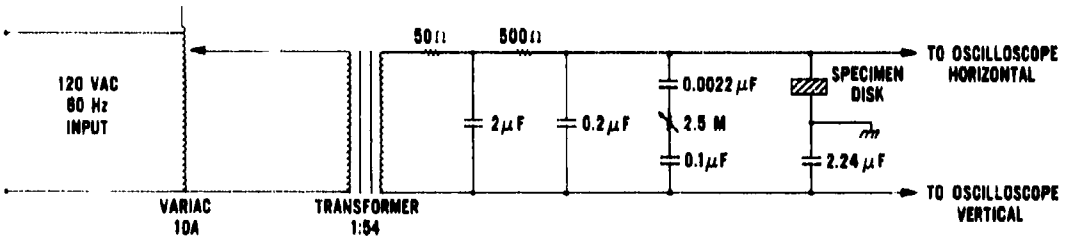

Figure 2. Schematic of Sawyer-Tower circuit for measuring a low-frequency hysteresis loop for a ferroelectric disk (Reference 8).

Measurements were made on two PZT disks. The average values for the remanent polarization vector and coercive field are 0.31 $\mu C/mm^2$ and 1.1 kV/mm, respectively. These values are in good agreement with the P_0 and E_c values reported in Table 1. Figure 3 shows a typical low-frequency hysteresis loop obtained for a PZT 56/44 disk.

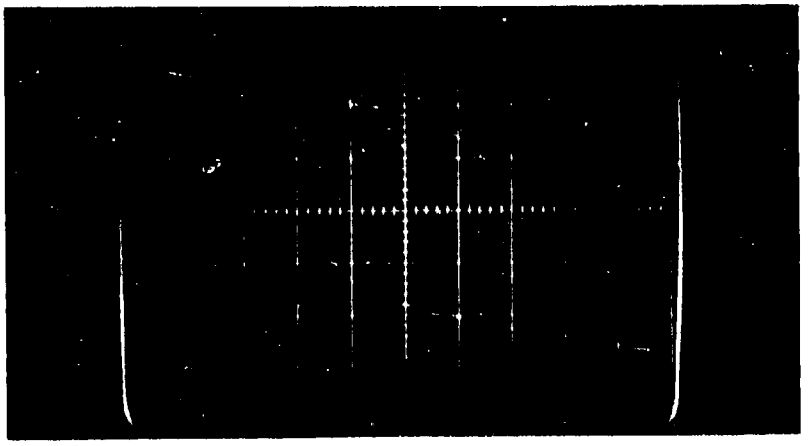

Figure 3. Oscilloscope record of low-frequency hysteresis loop for a PZT 56/44 disk. The vertical scale is 0.18 μC mm^{-2}/div, and the horizontal scale is 0.66 kV mm^{-1}/div.

Figure 4 is a schematic of the circuit that was fabricated for the high-frequency polarization reversal measurements. The circuit is divided into two parts: the main circuit shown on the right and the thyratron drive circuit shown on the left. In the main circuit, the 0.1-μF source capacitor (Plastic Capacitors, Inc., nonpolarized oil-filled paper-dielectric capacitor, hermetically sealed in a glass case) is charged to a voltage between 2 and 7 kV. When the thyratron switch is closed, the source capacitor is placed in parallel with the specimen disk, and a negative potential is applied to it. The thyratron drive circuit provides a fast-rising pulse for closing the thyratron switch. The voltage across the PZT specimen and the displacement current in the circuit are measured after the thyratron switch is closed. If the disk remanent polarization vector is initially pointing down in the figure, then it will be reversed by the negative voltage; if the polarization vector is initially pointing up in the figure, then it will not be reversed but cycled to a high-field saturation value. The data consist of a series of voltage and associated current pulses for different source capacitor voltage settings. The recording oscilloscopes were located in an electromagnetic-shielded room, and double-shielded coaxial signal cables were used for the voltage and current probes in order to minimize electromagnetic interference. For these measurements (as for the low-frequency measurements), a PZT disk was placed between two 12.7-mm-diameter brass electrodes and immersed in transformer oil.

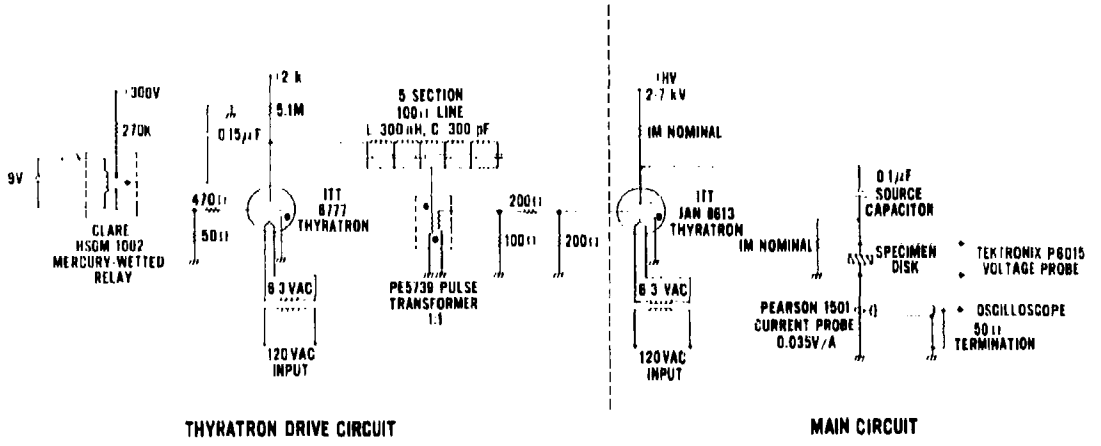

Figure 4. Schematic of circuit for performing polarization reversal measurements on PZT disks under high-field and high-frequency conditions.

Prior to performing the polarization reversal measurements on the PZT disks, a series of measurements was performed for the pulse charging of a 2.2-nF ceramic capacitor (6 kV maximum voltage rating). This was done in order to check the operation of the circuit for a nonferroelectric material with a capacitance similar to the 3.6-nF low-frequency capacitance of the PZT disk. Figure 5 shows the voltage and current pulses for a source capacitor voltage of 3 kV. The voltage pulse rises to a peak of about 5 kV in about 0.08 μs and then slowly decays to about 3.5 kV. A peak voltage obtained from the area under the current-time pulse agrees with the measured peak voltage to within about 10%. The voltage spike observed at 0.10 μs arises from an inductive transient caused by the current rapidly switching to zero due to the diode action of the thyratron. The initial increase in the voltage pulse above the source capacitor voltage can be explained as due to stray inductance in the circuit. Circuit analysis calculations for a series circuit consisting of a switch, a 0.1-μF source capacitor charged to 3 kV, a 2-nF load capacitor, an inductor, and a small resistor showed that for an inductance of 200 nH and a resistance of 3 Ω the initial voltage pulse on the 2-nF load capacitor increased to about 5 kV in 0.06 μs when the switch was closed. This calculated peak voltage and risetime are in good agreement with the measured values.

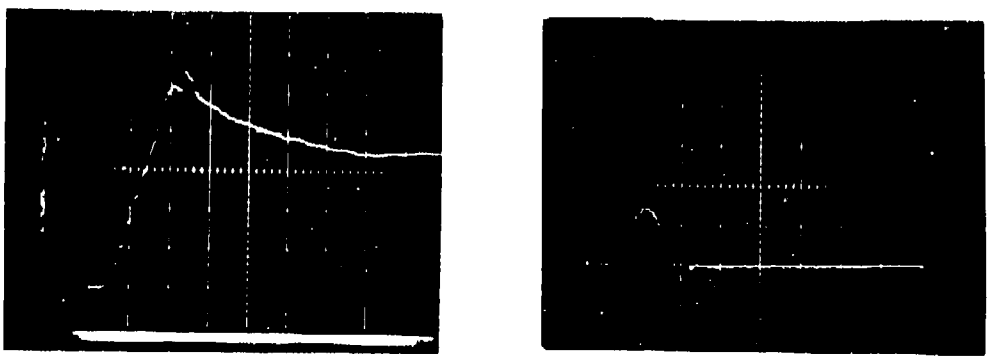

(a) (b)

Figure 5. Voltage and current records for pulse charging a 2.2-nF nonferroelectric ceramic capacitor. The 0.1-μF source capacitor voltage was 3 kV prior to closing the thyratron switch. (a) Voltage pulse. The vertical scale is 1 kV/div and the horizontal scale is 0.05 μs/div. (b) Current pulse. The vertical scale is 143 A/div and the horizontal scale is 0.05 μs/div.

Table 2 lists the results of the high-frequency polarization reversal measurements on the PZT 56/44 disks. Due to the destructive nature of these experiments, a specimen disk was used in only one measurement. In those experiments in which electrical breakdown occurred, an examination of the specimen disks indicated a discolored region either through the specimen or around the edge of the specimen. Breakdown through the specimen caused it to crack into two or more pieces. Each PZT disk was pulsed a second time after the initial polarization reversal measurement. Figure 6 shows the voltage and current pulses for one of these experiments. The PZT specimen responded essentially like an ordinary capacitor since the polarization vector was just cycled to a saturation value and back again to the remanent value. A 2.3-nF high-frequency, high-field capacitance value is obtained for the PZT disk from the measured peak voltage and area under the current-time pulse prior to electrical breakdown.

Figures 7 and 8 give the electric field and current pulses, respectively, for the polarization reversal measurements. The estimated uncertainty in these curves is 5 to 10%. Appendix A contains the oscilloscope records from which these curves were

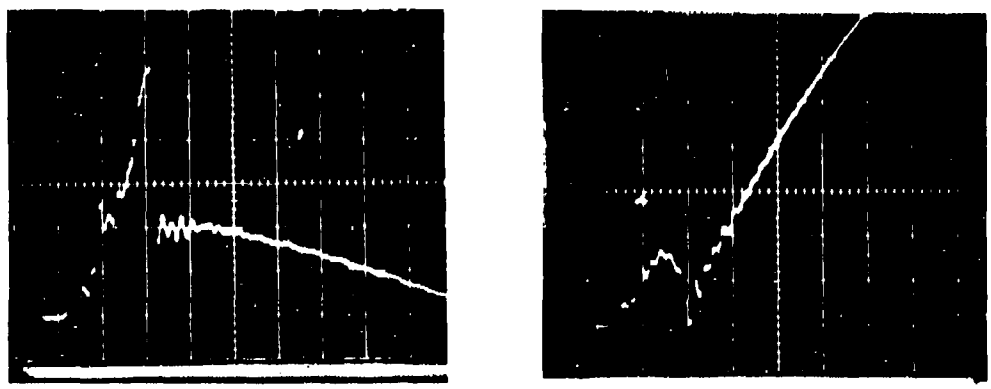

(a) (b)

Figure 6. Voltage and current records for pulse charging a PZT 56/44 disk for a source capacitor voltage of 7 kV. (a) Voltage pulse. The vertical scale is 2 kV/div and the horizontal scale is 0.05 μs/div. (b) Current pulse. The vertical scale is 286 A/div and the horizontal scale is 0.05 μs/div. Electrical breakdown occurred in the disk at 0.10 μs for an electric field of about 15 kV/mm. A voltage pulse (for a 7-kV capacitor voltage) that was initially applied to the disk reversed the remanent polarization vector and caused electrical breakdown.

obtained. The high-frequency oscillations that occurred on the initial part of some of the measured pulses were removed by averaging the amplitude of the oscillation. The electric field curves initially increase in a linear manner for about 0.04 μs and then level off at the coercive field value before increasing again. Table 2 lists the initial slope and coercive field values for each of the shots. The coercive field values range from 2.8 to 6.3 kV/mm. The time at which the electric field is near the coercive field value is related to the time required for domain switching to occur in the specimen. This time decreases with increasing coercive field. Table 2 also lists the peak electric fields and their times of occurrence. The results show that the peak electric field increases as the time to the peak electric field decreases.

Table 2. Results of polarization reversal experiments.

Specimen No.	Source Capacitor Voltage (kV)	Specimen Thickness[a] (mm)	Effective Specimen Diameter[b] (mm)	Initial Slope of Electric Field (kV $mm^{-1}/\mu s$)	Initial Slope of Current Pulse (kA/μs)	Coercive Field (kV/mm)	Time to Reduce Polarization to Zero (μs)	Peak Current (A)	Time of Peak Current (μs)	Peak Electric Field (kV/mm)	Time of Peak Electric Field (μs)	Current at Peak Electric Field (A)
1	2	0.752	12.7	44	3.0	2.8	0.29	157	0.29	2.8	0.43	153
2	3	0.754	12.7	72	4.4	3.4	0.17	386	0.23	5.2	0.33	55
3	4	0.754	12.7	100	5.8	4.3	0.13	617	0.19	9.6[c]	0.26[c]	0[c]
4	6	0.757	12.7	106	6.7	4.9	0.11	940	0.16	10.8[c,d]	0.19[c]	553[c]
5	7	0.749	12.7	157	8.5	6.3	0.10	1120	0.14	15.6[c]	0.17[c]	661[c]

[a]Measured at the edge of the disk; does not include the thickness of the fired-on silver electrodes.
[b]Diameter of brass electrodes that were placed in contact with the specimen disk.
[c]Electric field, current, and time just before electrical breakdown.
[d]Extrapolated electric field; peak of voltage pulse was not recorded.

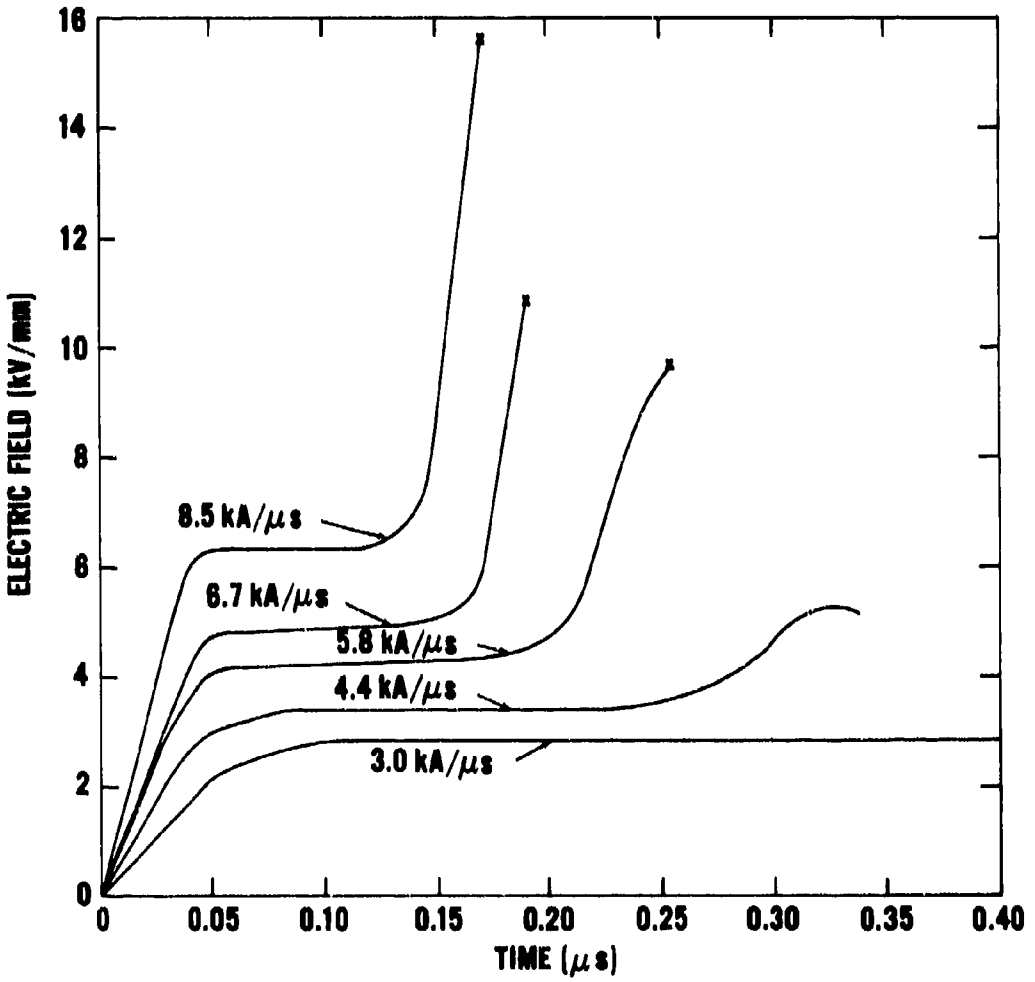

Figure 7. Polarization-reversal electric field curves for PZT 56/44 disks as a function of increasing source capacitor voltage. The curves are labeled with the initial slopes of the associated current-time pulses. The crosses indicate electrical breakdown in the disks.

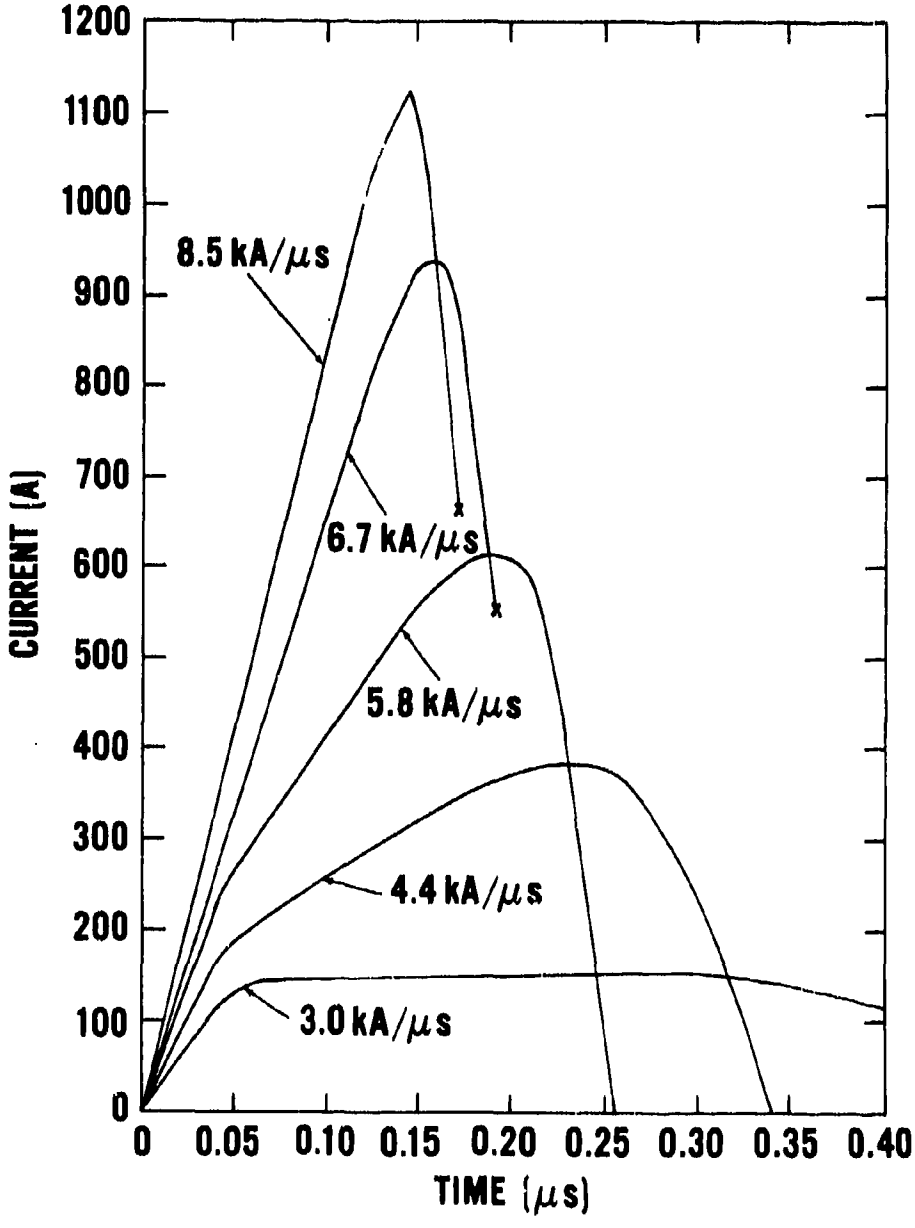

Figure 8. Polarization-reversal current pulses for PZT 56/44 disks as a function of increasing source capacitor voltage. The curves are labeled with the initial slopes of the pulses. The crosses indicate electrical breakdown in the disks.

The current pulses also initially increase in a linear manner for about 0.04 μs and then increase at a slower rate to a peak value. The peak value corresponds to the time when the electric field begins to exceed the coercive field. Table 2 also lists the peak currents and their times of occurrence. As the peak current increases, the time to peak current decreases. The range of initial slopes for the current pulses (3.0 to 8.5 kA/μs) is essentially the same as the range of initial slopes of the current pulses for the shock-depoled PZT 56/44 disks (presented in Section V). This allows an estimate to be made for the electric field ahead of the shock front in a shock-depoled PZT disk. This electric field will be taken as the field whose corresponding initial current slope equals the initial current slope for the shock-depoled disk. The initial charge release (area under the initial part of current-time pulse), and hence the decrease in the electric displacement vector, is the same for both cases.

Figure 9 shows the high-frequency electrical depoling paths for the polarization reversal measurements. Shown for comparison is half of a depoling path for a slow hysteresis loop (60-sec cycle, data provided by Gulton Industries, Inc.). This figure shows that the depoling path becomes wider as the coercive field increases. The largest coercive field is over six times the slow-loop coercive field. Plumlee[9,10] has performed high-frequency, high-field polarization reversal measurements on various compositions of PZT ferroelectric ceramics. Square-wave pulse fields with amplitudes as high as 13 kV/mm and durations from 0.01 to 3 μs were used to obtain depoling paths with coercive fields up to about ten times the slow-loop coercive field.

The depoling path curves in Figure 9 show that the times required to reduce the polarization vector to zero (corresponding to a change in electric displacement of 0.31 $\mu C/mm^2$) decrease as the initial current pulse slopes increase. These times (listed in Table 2) decrease from about 0.29 to 0.10 μs. For the first 0.04 μs of these depoling paths, the electric displacement decreases about 7 to 16% as the initial slopes of the current pulses increase from 3.0 to 8.5 kA/μs. For times greater than 0.04 to 0.05 μs the change is more rapid since domain switching occurs and the polarization vector reverses direction.

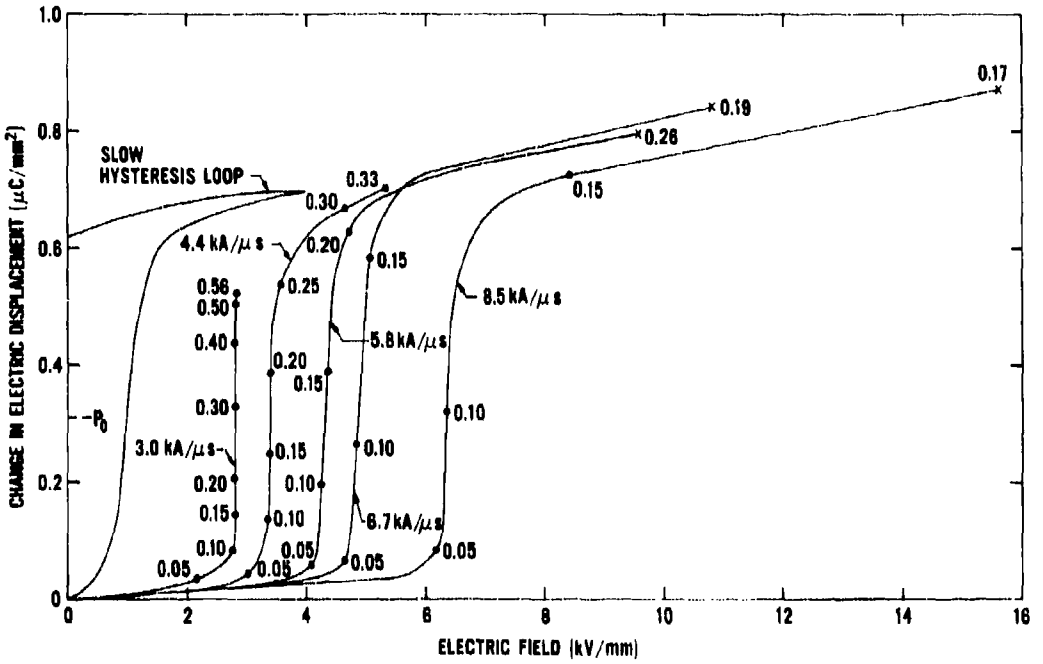

Figure 9. Change in electric displacement versus electric field for PZT 56/44 disks. These depoling path curves were constructed from the voltage and current pulses for the polarization reversal measurements. The curves are labeled with the initial slopes of the current-time pulses. Representative times in microseconds are shown on the curves. The crosses indicate electrical breakdown in the disks.

IV. EXPERIMENTAL TECHNIQUE FOR SHOCK-DEPOLING MEASUREMENTS

The shock depoling of the PZT 56/44 ferroelectric disks was performed with a 40-mm-bore diameter gas gun.[11] A schematic of the muzzle region of the gun is shown in Figure 10. A PZT target assembly is mounted on the end of the gun for impacting. The barrel is evacuated to about 0.1 Pa to minimize gas-cushion effects between the impactor and target faces at impact. The three charged velocity pins in

the side of the barrel and the charged trigger pin in the target assembly are used to measure an average projectile velocity at impact.

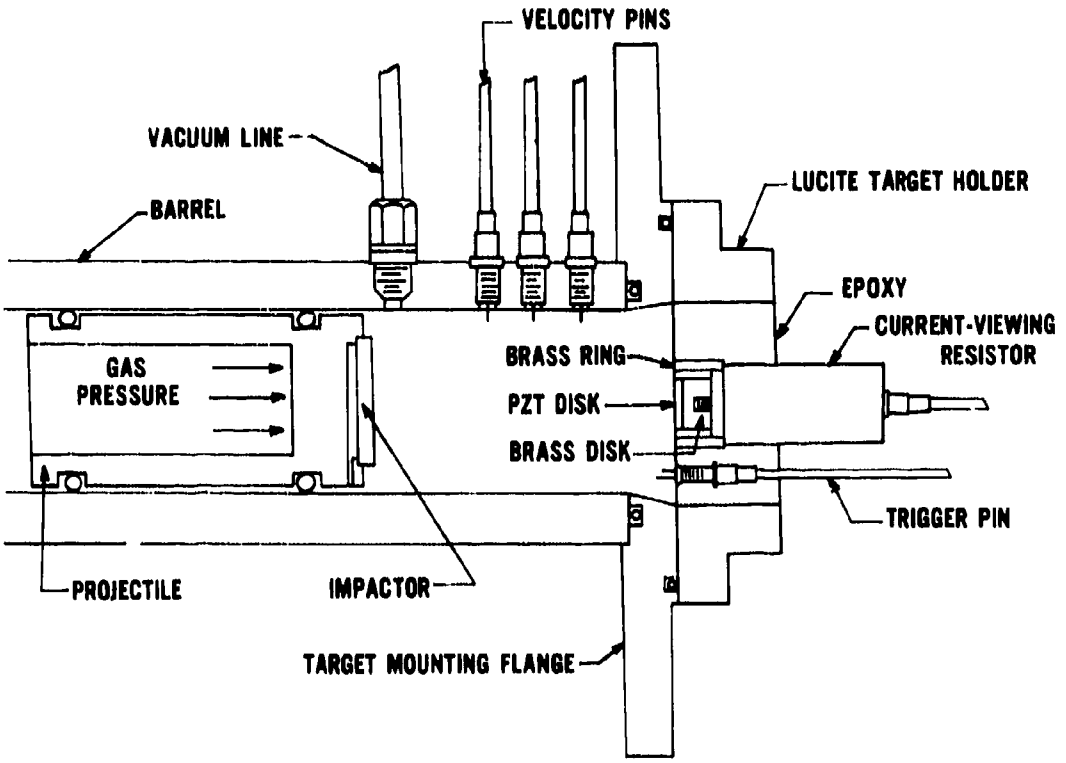

Figure 10. Schematic of muzzle region of gas gun showing the details of the target assembly for the axial-current-mode depoling of a PZT disk.

A procedure similar to that described in Reference 3 was followed for the fabrication of a PZT target assembly. The first step in the fabrication procedure is to lightly lap the electrode surfaces of the PZT disk with 0.3-μm lapping film (3M Company) to ensure a good electrical bond. The thickness of the disk is measured

with a micrometer on the electroded surfaces of the disk and on the nonelectroded annular region of the disk. Silver-loaded conductive paint (GC Electronics Silver Print No. 21-1) is used to attach one of the electrodes of the PZT disk to a brass (nonleaded Naval brass) backup disk. The positive PZT electrode is attached to the backup disk for an antiparallel orientation shot, and the negative electrode is attached for a parallel orientation shot. The surfaces are pressed together to minimize the thickness of the conductive paint layer. The thickness of the layer is about 3 μm. Brass is used for the backup material to provide an approximate impedance match to the PZT disk and therefore minimize the reflection of the initial shock wave from the PZT-brass interface. The brass disk has a nominal diameter of 12.7 mm and a thickness of 6.4 mm. An 8-32 UNF threaded hole, 4.8 mm deep in the back surface of the backup disk is used for attaching a current-viewing resistor (CVR).

The diameter of the PZT disk is reduced to the diameter of the backup disk by removing the nonelectroded outer surface through grinding and lapping. The final diameter of the PZT-brass composite disk is measured. This disk is then centered inside and attached to a brass ring with three beads of epoxy (Miller-Stephenson 828V-TETA). The disk and ring are supported on a flat granite surface plate to ensure that the face of the PZT disk and the end of the ring are in the same plane. The brass ring has an inner and outer diameter of 14.6 mm and 19.1 mm, respectively, and a height of 10.8 mm. The epoxy beads, which are spaced approximately 120° apart, attach the inner cylindrical surface of the brass ring to the outer cylindrical surface of the brass disk.

The next step in the fabrication procedure is the preparation of the target assembly for an epoxy pour. The assembly is supported on a granite surface plate that has been coated with a thin film (less than 0.25 μm) of fluorocarbon mold release. The PZT unit consisting of the PZT disk with inner and outer brass electrodes is centered with a special fixture inside a Lucite target holder.

The fixture also supports an oscilloscope trigger pin (Microdot Part No. 031-0050-0001) which has been attached to the end of a thin rod. The target holder has an inner and outer diameter of 45.7 mm and 88.9 mm, respectively, and an inner and outer flange thickness of 19.1 mm and 9.55 mm, respectively. Cylindrical weights are placed on the special fixture and the outer flange of the target holder to ensure that the PZT unit and target holder are in uniform contact with the surface plate. A nylon screw is placed in the threaded hole of the backup disk so that no epoxy will get into the hole. Figure 11 shows a PZT target assembly that is ready for an epoxy pour. Vacuum degassed epoxy is injected inside the target holder and into the region between the inner and outer brass electrodes

to a height of about 7 mm. The target assembly is then covered with a bell jar for additional vacuum degassing to remove any air trapped during injection of the epoxy. After the epoxy has cured, the target assembly is removed from the granite surface plate by gently tapping the edge of the target cup with a weight. If necessary, the height of the epoxy between the brass ring and disk is trimmed until the epoxy height is flush with the height of the brass disk. Lapping film and acetone-soaked Kimwipes are used to remove any excess epoxy from the impact surface of the target assembly.

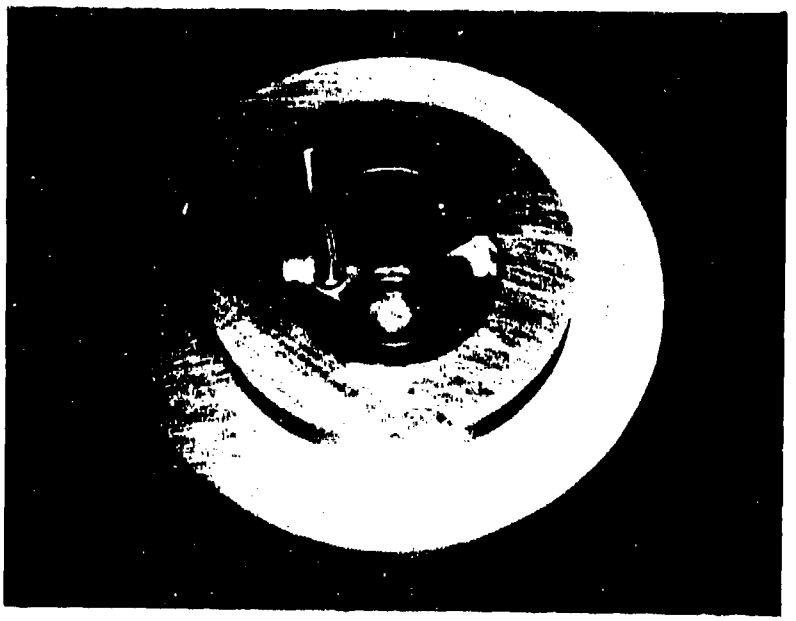

Figure 11. PZT target assembly on granite surface plate before epoxy pour.

The center conductor of a coaxial, noninductive, 0.05-Ω CVR (T&M Research Products No. A-5-05, 1000-MHz bandpass frequency, 0.36-ns risetime, 5-J maximum energy rating) is screwed into the threaded hole in the backup disk until the CVR cylindrical ground conductor contacts the brass ring. Conductive paint was placed

inside the threaded hole and on the back surface of the ring to insure good electrical contact between the CVR and the PZT unit. The circuit for the coaxial PZT unit is completed by connecting the impact surface of the PZT disk to the brass ring with a thin film (approximately 20 μm) of conductive paint.

The final step in the fabrication of a PZT target assembly consists of setting the height of the center and ground conductors of the oscilloscope trigger pin. Indium solder is used to extend the height of these conductors beyond the face of the PZT unit. Using the probe of a vernier height gauge, the heights of the center and ground conductors are adjusted to be approximately 0.70 and 0.75 mm, respectively, above the impact surface of the PZT unit.

Figure 12 shows a completed PZT target assembly mounted on the gun muzzle. RG-188/U 50-Ω coaxial cables carry the signals from the CVR and trigger pin to the connector manifold located above the target mounting flange. The CVR signal was recorded with one oscilloscope directly and with two additional oscilloscopes using 100X attenuation pickoff probes (Tektronix Type P6057). The oscilloscopes were operated at separate horizontal sweep speeds of 0.05, 0.1, and 0.2 μs.

Twenty shock-depoling experiments were performed. Both antiparallel and parallel orientation shots were performed for a given shock stress so that the orientational dependence of the short-circuit current could be determined. Table 3 gives the impactor and specimen parameters for these shots. Polymethyl methacrylate (PMMA), quartz, and nickel were used as impactor materials. The average specimen thickness was 0.756 mm. The projectile impact velocity listed in the last column of the table has an estimated uncertainty of 0.5%.

V. RESULTS AND DISCUSSION

Table 4 summarizes the experimental results for the antiparallel and parallel orientation measurements. The shock stresses in the PZT disks were calculated using the Hugoniot equation of state for PZT 52/48[12] material (since the Hugoniot for the PZT 56/44 material has not been determined) and the Hugoniots for the impactor materials PMMA,[13] quartz,[14] and nickel.[15] The density of the PZT 52/48 material is 7.58 Mg/m^3. (PZT 52/48 is a solid solution containing 52 mole % lead zirconate and 48 mole % lead titanate with niobium as a minor added constituent.) A primary depoling current pulse was recorded for each shot. One or more secondary pulses that immediately followed the primary pulse, and a repoling pulse

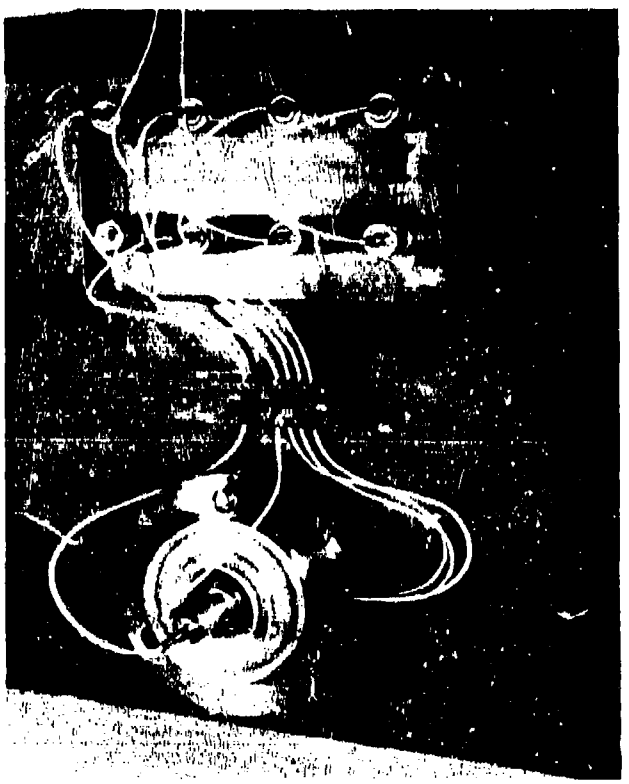

Figure 12. PZT target assembly on gas gun muzzle prior to firing gun.

that occurred about 1 μs after the primary pulse were also recorded. Appendix B contains the oscilloscope records for each shot. The peak current, time of peak current, pulse duration, and charge release were obtained for each pulse. Also, the initial slope of the primary current pulse was measured. The estimated uncertainty in these values is 5 to 10%.

Table 3. Impactor and specimen parameters for shock-depoling experiments.

Shot No.	Impactor Material	Impactor Diameter (mm)	Impactor Thickness (mm)	Specimen Orientation	Specimen Diameter (mm)	Specimen Thickness[a] (mm)	CVR Value (Ω)	Impactor Velocity[b] (km/s)
38	PMMA[c]	25.4	3.202	AP[d]	12.65	0.762	0.0510	0.218
42	quartz[e]	25.43	3.218	AP	12.68	0.762	0.0493	0.144
36	quartz	25.43	3.218	AP	12.64	0.757	0.0504	0.224
49	quartz	25.42	3.213	AP	12.58	0.747	0.0501	0.285
44	quartz	25.43	3.213	AP	12.62	0.754	0.0514	0.364
48	quartz	25.43	3.218	AP	12.63	0.744	0.0508	0.431
50	quartz	25.42	3.218	AP	12.55	0.760	0.0506	0.526
54	nickel[f]	25.4	3.18	AP	12.57	0.752	0.0500	0.387
52	nickel	25.4	3.18	AP	12.62	0.749	0.0510	0.459
53	nickel	25.4	3.18	AP	12.65	0.749	0.0511	0.565
39	PMMA	25.4	3.202	P[g]	12.57	0.767	0.0509	0.218
41	PMMA	25.4	3.202	P	12.53	0.757	0.0503	0.423
37	quartz	25.42	3.211	P	12.60	0.762	0.0507	0.221
45	quartz	25.43	3.218	P	12.60	0.760	0.0495	0.283
46	quartz	25.42	3.218	P	12.63	0.752	0.0506	0.367
47	quartz	25.42	3.198	P	12.53	0.762	0.0514	0.430
51	quartz	25.42	3.211	P	12.60	0.754	0.0504	0.426
55	nickel	25.4	3.18	P	12.63	0.757	0.0501	0.383
56	nickel	25.4	3.18	P	12.61	0.752	0.0508	0.459
57	nickel	25.4	3.18	P	12.66	0.765	0.0508	0.573

[a]Measured at the edge of the disk; does not include the thickness of the fired-on silver electrodes.
[b]Average value for three velocity intervals except for Shots 54 and 55, which are average values for two velocity intervals.
[c]Preshrunk Lucite purchased from Universal Plastics and Engineering Company, Inc., Rockville, MD.
[d]Antiparallel orientation.
[e]The quartz impactors were X-cut with approximately 25 kA of chrome/gold deposited on their entire surface. They were purchased from Valpey-Fisher Corporation, Holliston, MA.
[f]The nickel impactors were 98 wt. % pure nickel with a hardness of R_b 43. The measured ultrasonic longitudinal and shear wave velocities are, respectively, 5.74 km/s (for a center frequency of 9 MHz of a broadband pulse) and 3.00 km/s (for a center frequency of 2 MHz of a broadband pulse).
[g]Parallel orientation.

Table 4. Results of shock-depoling experiments.

Shot No.	Specimen Orientation	Calculated Shock Stress (GPa)	Initial Slope of Current Pulse[a] (kA/μs)	Peak Current (A)	Time of Peak Current (μs)	Pulse Duration (μs)	Charge Release[b] (μC/mm^2)	Time from Beginning of Current Pulse to Beginning of Repoling Pulse[c] (μs)	Peak Current of Repoling Pulse (A)	Time of Peak Current from Beginning of Repoling Pulse (μs)	Pulse Duration (μs)	Charge Release (μC/mm^2)
38[d,e]	AP[f]	0.7	1.3	146	0.14	0.27	0.186	1.02	-6	0.13	>0.15	< -0.004
				-28	0.32	0.10	-0.015					
				71	0.47	0.23	0.070					
				-10	0.63	0.14	-0.006					
42	AP	1.5	1.1	160	0.18	0.37	0.258	1.12	-24	0.24	>0.40	< -0.040
				22	0.53	0.25	0.025					
36	AP	2.2	5.1	282	0.08	0.24	0.257	1.15	-36	0.11	>0.27	< -0.045
				26	0.34	0.15	0.015					
49	AP	2.7	2.7	249	0.09	0.25	0.244	1.19	No measurements, only the beginning of the repoling pulse was observed.			
				19	0.33	0.12	0.012					
44	AP	3.3	3.9	234	0.10	0.29	0.260	1.19	-21	0.16	>0.17	< -0.016
				6	0.32	0.10	0.003					
48	AP	3.9	8.1	425	0.06	0.25	0.249	1.17	-19	0.10	>0.19	< -0.017
				7	0.30	0.09	0.007					
50[g]	AP	4.7	7.8	341	0.06	0.22	0.252	1.18	-15	0.13	>0.23	< -0.012
				5	0.31	0.12	0.003					
54[g]	AP	5.6	4.6	>580[h]	0.05	0.23	0.248	1.23	No measurements, only the beginning of the repoling pulse was observed.			
				7	0.33	0.04	0.001					
52	AP	6.8	2.5	184	0.10	0.27[i]	0.224	None observed in the 1.32 μs recording time after the beginning of the current pulse.				
				31	0.31	0.09	0.014					
53	AP	8.6	7.3	168	0.07	0.23[i]	0.192	None observed in the 1.34 μs recording time after the beginning of the current pulse.				
				21	0.25	0.07	0.009					
39	P[j]	0.7	1.5	149	0.13	0.26	0.180	1.10	-8	0.13	0.24	-0.009
				-51	0.34	0.12	-0.034					
				87	0.47	0.23	0.093					
				-9	0.69	0.16	-0.006					

Table 4. Results of shock-depoling experiments. (Continued)

Shot No.	Specimen Orientation	Calculated Shock Stress (GPa)	Initial Slope of Current Pulse[a] (kA/μs)	Peak Current (A)	Time of Peak Current (μs)	Pulse Duration (μs)	Charge Release[b] (μC/mm²)	Time from Beginning of Current Pulse to Beginning of Repoling Pulse[c] (μs)	Peak Current of Repoling Pulse (A)	Time of Peak Current from Beginning of Repoling Pulse (μs)	Pulse Duration (μs)	Charge Release (μC/mm²)
41[g]	P	1.5	1.5	231	0.13	0.27	0.241	None observed in the 1.46 μs recording time after the beginning of the current pulse.				
				17	0.39	0.21	0.020					
37	P	2.2	5.3	257	0.09	0.24	0.246	None observed in the 1.06 μs recording time after the beginning of the current pulse.				
				7	0.34	0.15	0.009					
45	P	2.6	5.7	259	0.09	0.27	0.271	1.18	-21	0.11	>0.11	< -0.009
				8	0.32	0.12	0.008					
46	P	3.3	7.4	371	0.07	0.23	0.250	1.15	-21	0.11	>0.11	< -0.007
				7	0.37	0.16	0.004					
47	P	3.9	7.0	374	0.07	0.19	0.281	1.15	-20	0.13	>0.13	< -0.012
				-39	0.24	0.14	-0.025					
				6	0.39	0.12	0.005					
51	P	4.7	5.3	306	0.09	0.25	0.253	1.12	-10[k]	0.10[k]	>0.10	< -0.003
				10	0.33	0.12	0.010					
55	P	5.5	8.6	320	0.07	0.25	0.247	None observed in the 1.32 μs recording time after the beginning of the current pulse.				
				9	0.31	0.14	0.006					
56	P	6.8	6.4	312	0.08	0.27	0.260	None observed in the 1.31 μs recording time after the beginning of the current pulse.				
				10	0.33	0.10	0.005					
57	P	8.8	21	417	0.05	0.24	0.257	None observed in the 1.23 μs recording time after the beginning of the current pulse.				
				7	0.30	0.09	0.006					

[a]The results for the primary and secondary pulses were obtained from the 0.1 μs/div horizontal-sweep-speed oscilloscope records.

[b]The charge release was obtained by averaging the area under the current-time pulses for the 0.1 μs/div and 0.2 μs/div horizontal-sweep-speed oscilloscope records.

[c]The results for the repoling pulses were obtained from the 0.2 μs/div horizontal-sweep-speed oscilloscope records.

[d]For all the shots one or more secondary pulses occurred in addition to the primary depoling pulse. The primary depoling pulse is listed first for each shot followed by the secondary pulses. The positive secondary pulses are probably caused by shock wave reflections at the PZT-brass backup interface into an incompletely depoled PZT disk. The negative secondary pulses may be caused by partial stress relief occurring at the thin conductive layer between the PZT disk and brass backup. Some of the structure observed in the pulses may also be due to stray inductance effects in the circuit.

[e]In some of the shots the current records indicated a repoling pulse about a microsecond after the primary depoling pulse. The < sign for the charge release shows that the pulse was partially recorded. The repoling pulses are probably due to a stress relief wave propagating into the PZT disk from the back surface of the impactor disk or from the hole in the brass backup.

[f]Antiparallel orientation.

[g]For these shots the primary depoling pulse had a slowly rising ramp before the major part of the pulse occurred. The time of peak current and pulse duration were measured with respect to a zero time obtained from the intersection of an extrapolation of the initial slope of the major part of the pulse with the time axis. The extrapolated zero times for Shots 50, 54, and 41 are 0.06, 0.125, and 0.125 μs, respectively. The initial slope is for the major part of the pulse. The charge release includes the area under the entire current pulse. The reason for the slowly rising ramp may be stress wave-form tilt.[3]

[h]The peak current went off scale and was not recorded.

[i]For these shots the primary pulse did not go to zero prior to the appearance of the secondary pulse. The primary pulse duration was obtained from the intersection of an extrapolation of the trailing edge of the primary pulse and the time axis.

[j]Parallel orientation.

[k]A peak current was not achieved. This is the maximum current at the end of the recording time.

The initial slopes of the primary depoling current pulses show an increase with shock stress up to about 4 GPa. Above this stress, the slope values show considerable scatter. The values range from 1.1 to 8.6 kA/μs, except for Shot 57 which had a value of 21 kA/μs. As mentioned in Section III, this range of values is similar to the range of initial slopes of the current pulses for the polarization reversal measurements.

Figure 13 shows the peak current values for the primary pulses as a function of shock stress. Considerable scatter is evident, especially for stresses above 4 GPa. The average of the peak currents for the two orientations increases from about 120 A at 0.7 GPa to a constant value of 340 A beginning at about 3.5 GPa. The peak currents for the two orientations are similar (excluding the very large value for Shot 54, which is probably experimental in nature) except for the 6.8- and 8.8-GPa stress regions. At these shock stresses, the peak currents for the parallel orientation shots are near the average value, whereas the peak currents for the antiparallel orientation shots are about half the average value.

The peak current values for the positive secondary pulses for each orientation can also be compared. For the parallel orientation experiments, the peak current decreases from a value of about 90 A at 0.7 GPa to a constant value of about 8 A for stresses above 2.2 GPa. For the antiparallel orientation experiments, the peak current decreases from a value about 70 A at 0.7 GPa to an average value of about 6 A for stresses in the range from 3.3 to 5.6 GPa and then increases again to an average value of about 25 A for the 6.8- and 8.6-GPa shots.

At the lower shock stresses, the large-amplitude secondary pulses for both orientations are probably due to incomplete depoling of the PZT disk by the initial shock wave; a reflected shock wave from the PZT-brass interface would cause additional shock depoling to occur. For the 0.7-GPa shots, the average ratio of the peak current for the secondary depoling pulses to the primary depoling pulses is 0.54. For the 1.5-GPa shots, this ratio decreases to 0.11. For the higher shock stresses (excluding the 6.8- and 8.6-GPa antiparallel orientation shots), the average value for this ratio is 0.03, indicating that the initial shock wave essentially completely depoles the disk so that the reflected shock wave causes negligible additional depoling. For the 6.8- and 8.6-GPa antiparallel orientation shots, this ratio increases to about 0.15, indicating the effects of electrical breakdown and conduction in the PZT material.

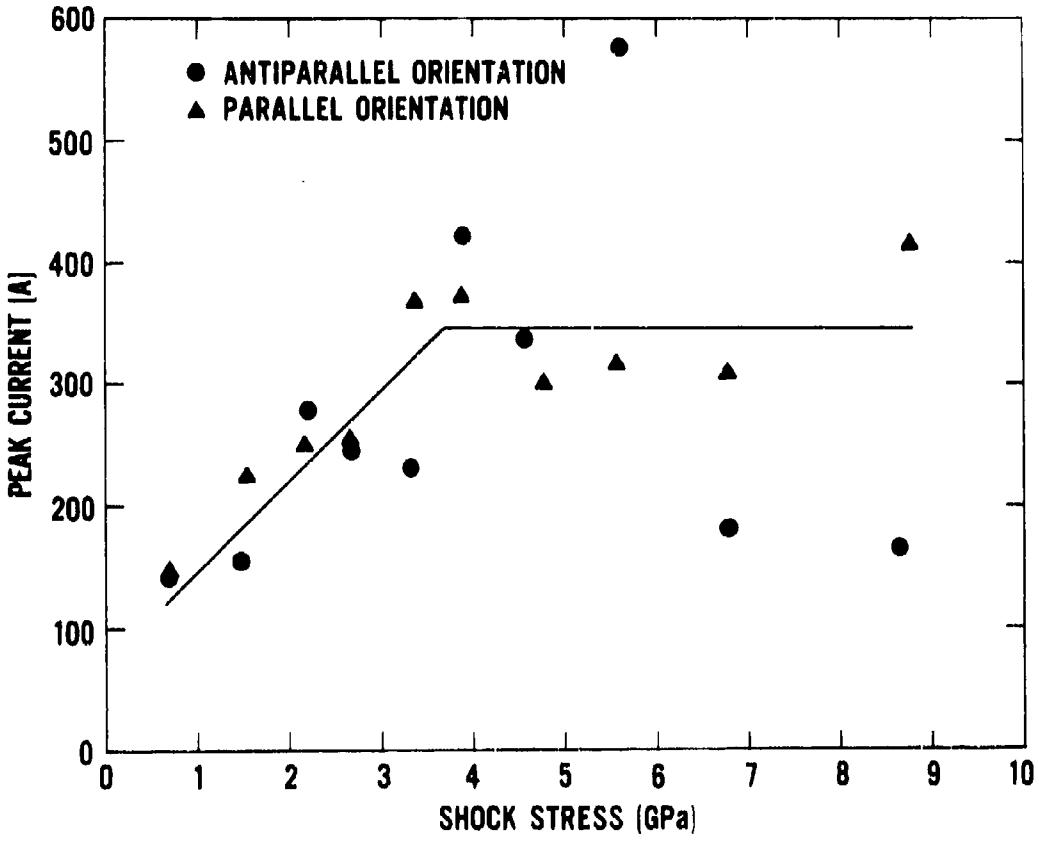

Figure 13. Peak current versus shock stress for PZT 56/44 disks. Each point represents the peak current for the primary depoling current pulse. The lines suggest trends in the data. The constant value is the average of the last five shots for each orientation.

Figure 14 shows the time of peak current values for the primary pulses as a function of shock stress. The average time decreases from about 0.16 μs at 0.7 GPa to a constant value of 0.07 μs beginning at about 3.5 GPa. This figure indicates that there are no large differences in the time of peak current for the two orientations. For the positive secondary pulses, the time of peak current for both orientations decreases from 0.47 μs at 0.7 GPa to an average value of 0.32 μs for

shock stresses greater than 2.2 GPa. The primary pulses for both orientations had durations ranging from 0.19 to 0.37 μs with an average value of 0.25 μs. The majority of the pulse durations were between 0.22 and 0.29 μs. The average value of the durations for the positive secondary pulses was 0.14 μs.

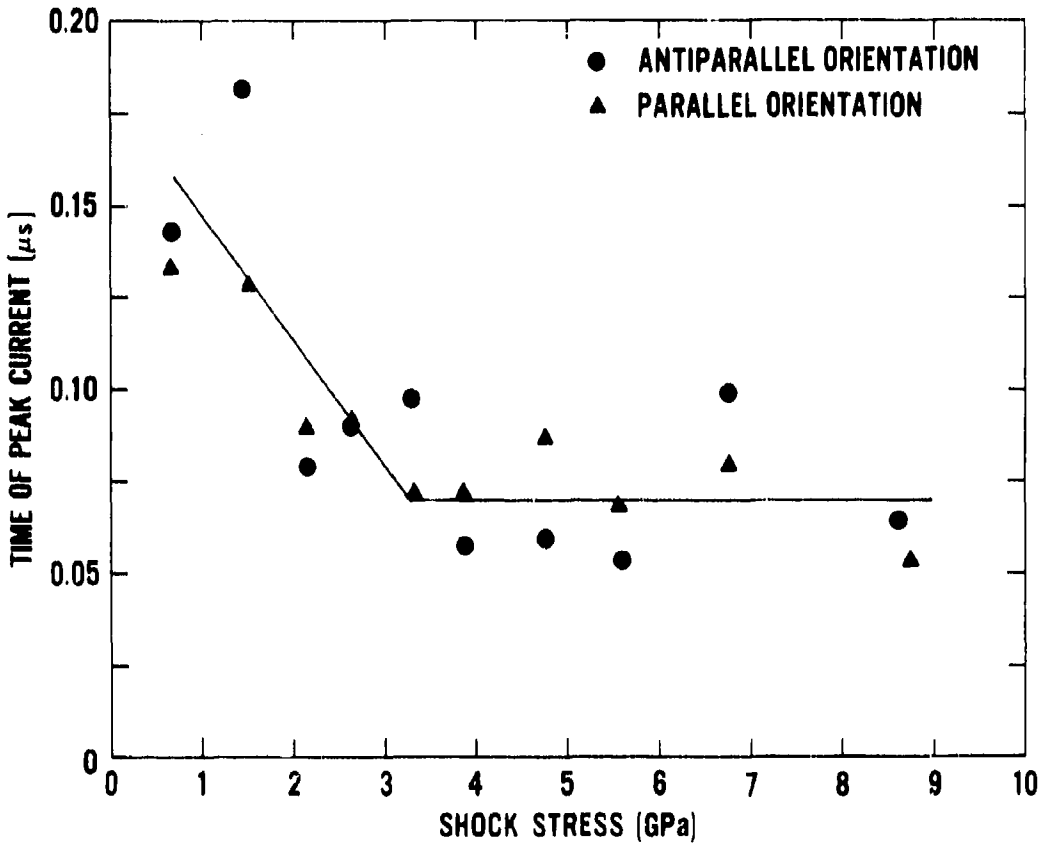

Figure 14 Time of peak current versus shock stress for PZT 56/44 disks. Each point represents the peak current for the primary depoling current pulse. The lines indicate trends in the data. The constant value is an average of the last five shots for each orientation.

The peak current, time of peak current, and pulse duration values in Table 4 depend to some extent, especially at low projectile velocities, on the impact planarity angle (tilt) between the impactor and specimen faces. The impactor-specimen tilt angle causes the stress wavefront in the PZT specimen to have an even larger tilt (factor of 10 to 20).[3] For a sufficiently large impactor-specimen tilt angle, the time for the entire front face of a thin PZT disk to come under shock compression (closure time) could be an appreciable fraction of the shock transit time in the disk. Halpin[3,6] has shown that the shape of the primary depoling current pulse from a thin PZT disk is dependent on the tilt angle even though the charge release or total area under the current-time pulse is essentially independent of this angle. As the tilt angle increases, the pulse spreads in time and its amplitude decreases, but the area remains constant. The tilt angle was not measured directly in any of the PZT shots. A tilt angle was measured in a separate shot using the same impactor and target preparation procedures that were used in the PZT shots. The measured tilt angle for this shot was 1.4 mrad. Assuming this tilt angle is representative for the PZT shots, the average ratio of the closure time to the time of peak current for the shots is about 0.63.

The ratios of the charge release for the positive secondary pulses to the charge release for the primary pulses show a similar behavior when compared to the ratios of the peak currents that were obtained earlier. For the 0.7-GPa shots, the charge release ratio is 0.45. The ratio decreases to 0.09 for the 1.5-GPa shots. For the higher shock stress (excluding the 6.8- and 8.6-GPa antiparallel orientation shots), the average ratio is 0.03. For the 6.8- and 8.6-GPa antiparallel orientation shots the ratio increases to 0.06.

Figure 15 gives the charge release for the primary depoling pulses versus shock stress. The points show less scatter when compared with Figures 13 and 14 since the charge release is less influenced by impact tilt than the peak current or time of peak current. The initial slope of the charge release - stress curve is 270 pC/N. This value can be compared with the piezoelectric charge coefficient of 400 pC/N from Table 1, which is defined only for nonpermanent depoling stresses that are a small fraction of a gigapascal. The total available charge was not released in any of the shots. In the 1.5- to 5.6-GPa stress range the average charge release is about 82%. The average charge release for the two orientations agrees up to 5.6 GPa. For the higher stress levels, the charge release for the antiparallel orientation shots begins to decrease. The average charge release for the positive secondary pulses is about 3% of the available charge for the shots in the 1.5- to 8.8-GPa stress range.

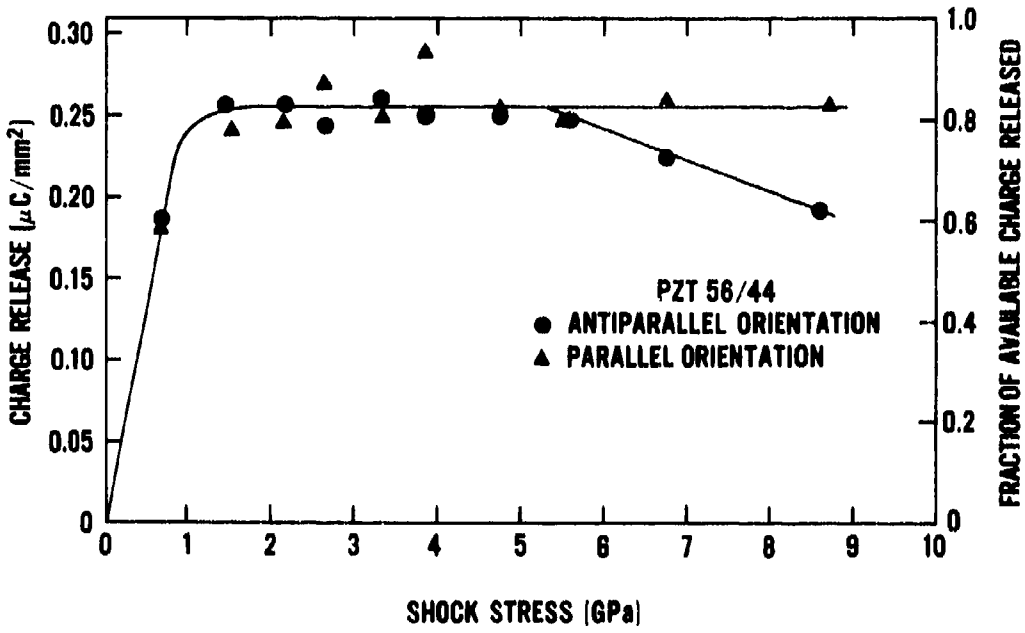

Figure 15. Charge release versus shock stress for PZT 56/44 disks. Each point represents the charge release for the primary depoling current pulse. The constant value is the average of the shots of both orientations in the 1.5- to 5.6-GPa stress range.

Figures 16 through 25 are a comparison of the primary current pulses for the antiparallel and parallel orientation shots at a given shock stress. These figures were constructed by digitizing the oscilloscope current records obtained at a 0.10-μs sweep speed. The pulse shapes for the 0.7- and 1.5-GPa shots are approximately symmetrical about the peak. For these shots, the time of peak current is about 50% of the pulse duration. For the higher stress shots, a slowly decaying tail is evident on the pulses, and the pulse shapes are nonsymmetrical. The time of peak current occurs at earlier times and is, on the average, about 31% of the pulse duration. These figures show that no significant differences in the pulse shapes for the two orientations occur (excluding experimental variations) for stresses up to 5.6 GPa. Large orientation-dependent differences occur in the pulse shapes for both the 6.8- and 8.8-GPa stress regions. The antiparallel orientation shots showed electrical breakdown effects. For the 6.8-GPa stress level, the peak current and charge release for the primary pulses are reduced by 41% and 14%, respectively, for the

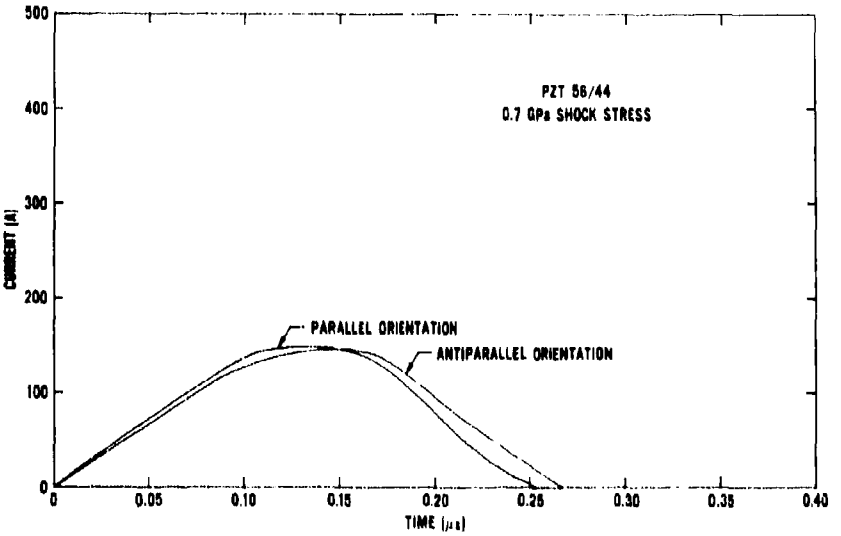

Figure 16. Current pulses for the antiparallel and parallel orientation shots at a shock stress of 0.7 GPa.

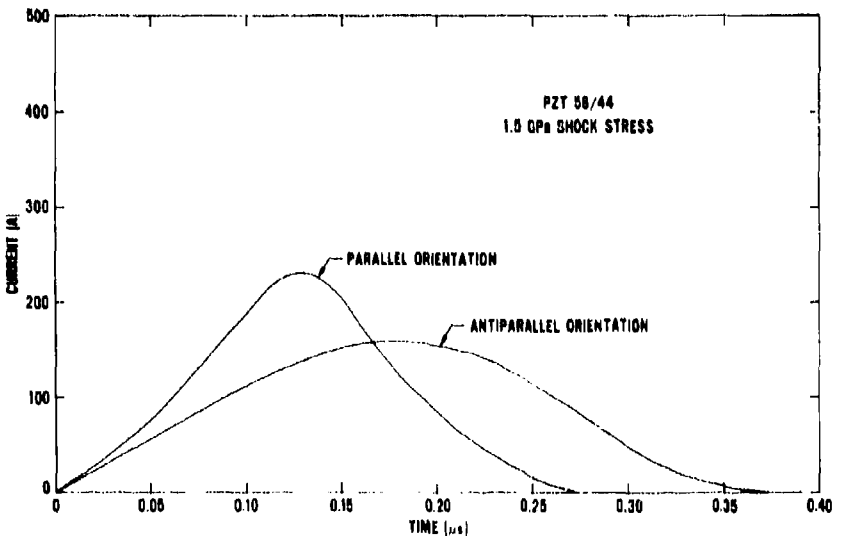

Figure 17. Current pulses for the antiparallel and parallel orientation shots at a shock stress of 1.5 GPa. At this low stress level, the difference in the pulse shapes can probably be attributed to stress waveform tilt.

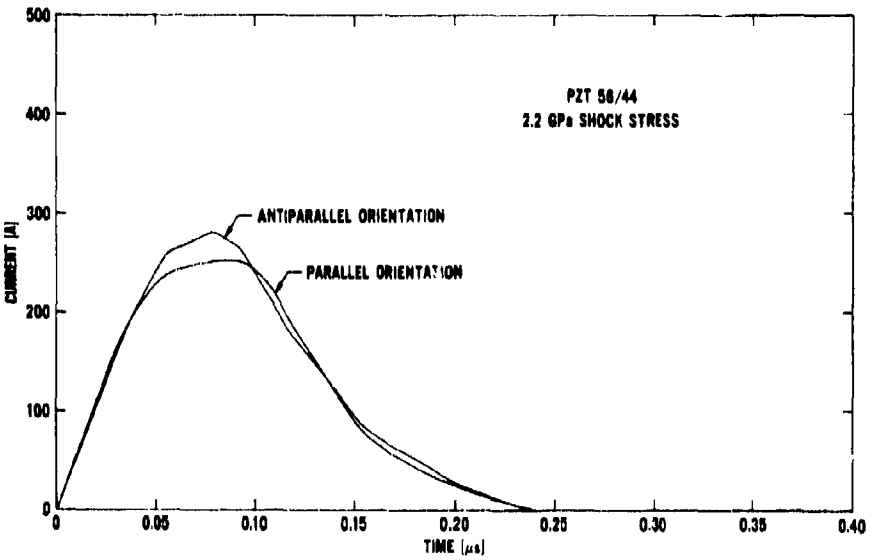

Figure 18. Current pulses for the antiparallel and parallel orientation shots at a shock stress of 2.2 GPa.

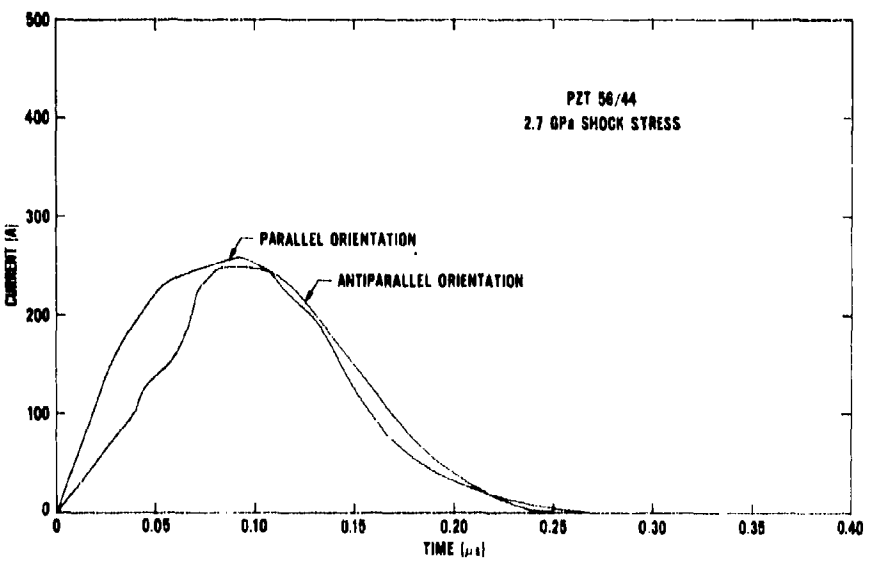

Figure 19. Current pulses for the 2.7-GPa antiparallel orientation shot and 2.6-GPa parallel orientation shot.

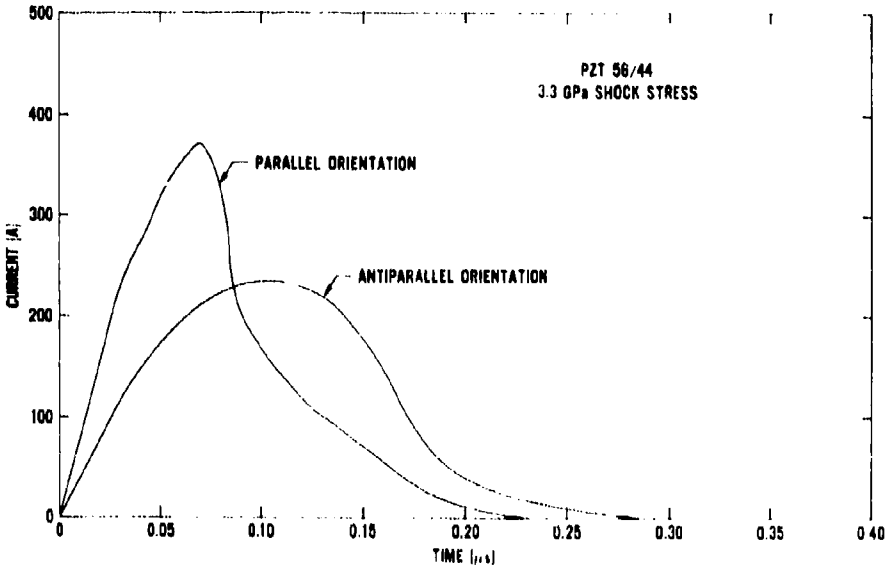

Figure 20. Current pulses for the antiparallel and parallel orientation shots at a shock stress of 3.3 GPa.

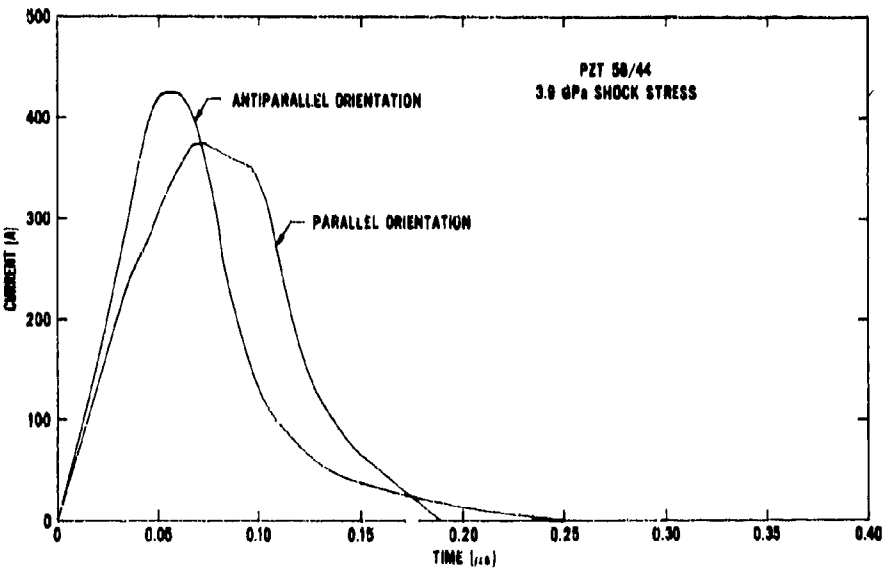

Figure 21. Current pulses for the antiparallel and parallel orientation shots at a shock stress of 3.9 GPa.

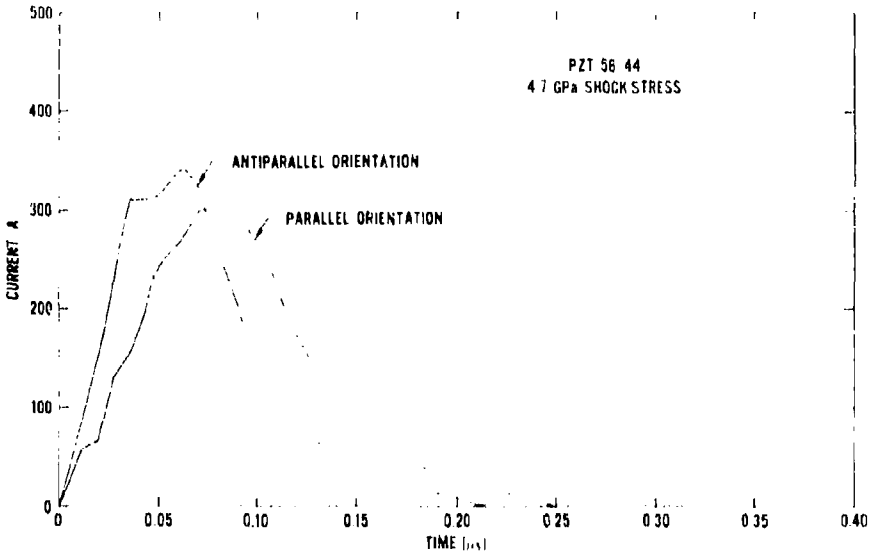

Figure 22. Current pulses for the antiparallel and parallel orientation shots at a shock stress of 4.7 GPa.

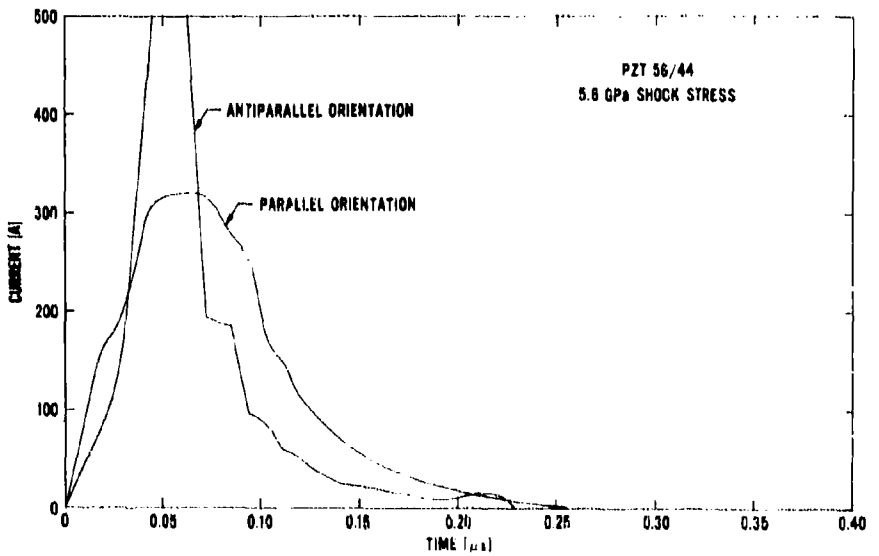

Figure 23. Current pulses for the 5.6-GPa antiparallel orientation shot and the 5.5-GPa parallel orientation shot. The peak of the antiparallel orientation shot (>580 A) was off scale and was not recorded. The large difference between the pulse shapes for these shots is probably experimental in nature since the charge release is the same for both shots.

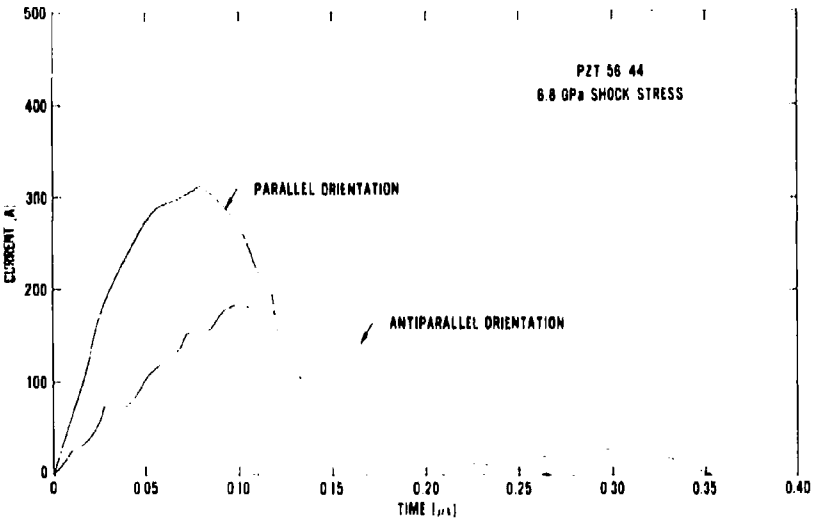

Figure 24. Current pulses for the antiparallel and parallel orientation shots at a shock stress of 6.8 GPa. Both the primary and secondary current pulses are shown for the antiparallel orientation shot. The lower peak current and reduced charge release for this shot indicate electrical breakdown in the PZT specimen.

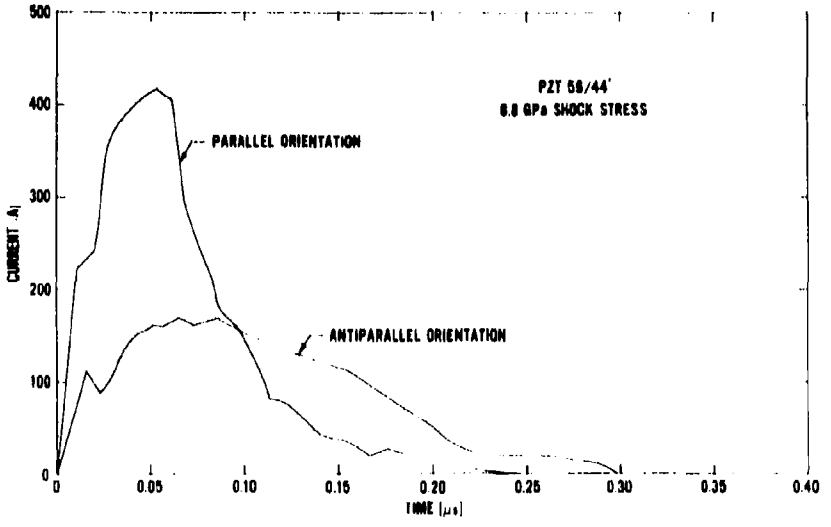

Figure 25. Current pulses for the 8.6-GPa antiparallel orientation shot and the 8.8-GPa parallel orientation shot. Both the primary and secondary current pulses are shown for the antiparallel orientation shot. The lower peak current and reduced charge release indicate electrical breakdown in the PZT specimen.

antiparallel orientation compared with the parallel orientation. For the 8.8-GPa region, the reduction was 60% and 25%, respectively. In contrast, for the secondary pulses in both stress regions, the peak current and charge release values for the antiparallel orientation shots are greater than the values for the parallel orientation shots. The reason for this recovery is not known. At these stress levels it is expected that the amplitude of the secondary pulses would be independent of the orientation of the PZT disk, since the magnitude of the initial shock wave would cause essentially complete depoling of the disk, independent of electrical breakdown. For both stress regions, the extrapolated primary pulse duration (an extension of the decreasing portion of the primary current pulse to the time axis) for the antiparallel orientation shot is in agreement with the primary pulse duration for the parallel orientation shot.

Figures 26 and 27 are a comparison of the current pulses for the antiparallel and parallel orientation shots, respectively. These figures show that as the shock stress increases the peak current increases and shifts to earlier times until electrical breakdown occurs. Even though the pulse shapes change significantly as the shock stress increases, the total charge release is essentially constant (see Figure 15) for shock stresses above 1.5 GPa (excluding the 6.8- and 8.6-GPa antiparallel orientation shots).

The average pulse duration for the shots is about 0.25 μs. This value is significantly larger than a transit time calculated from either the PZT 56/44 ultrasonic longitudinal wave velocity or the PZT 52/48 elastic shock wave velocity. Table 5 gives the results of the ultrasonic velocity measurements for PZT 56/44 disks. A transit time of 0.17 μs is obtained for the average PZT disk thickness of 0.756 mm and the longitudinal wave velocity in Table 5. The PZT 52/48 elastic wave velocity increases from 3.49 km/s for 0.7 GPa to a constant value of 4.14 km/s for stresses of 2.2 GPa and above.[12] The resulting transit time decreases from 0.22 to 0.18 μs in this stress range. The corresponding elastic strain increases from 0.007 to 0.014. For stresses above 2.2 GPa, the PZT 56/44 and PZT 52/48 transit times agree within 10% although they are about 30% less than the average pulse duration. Figures 26 and 27 indicate that, for the majority of the current pulses (excluding the stress levels of 0.7 and 1.5 GPa for both orientations), about 5 to 10% of the charge in a given primary pulse is released between the calculated transit time and average pulse duration.

Several possible reasons may be considered for the longer-than-expected average pulse duration. Impact tilt may be one contributing factor, since it has been shown previously that tilt causes the pulse duration to increase.[3,6] This contribution should decrease as the projectile velocity increases. Another factor to be considered is the

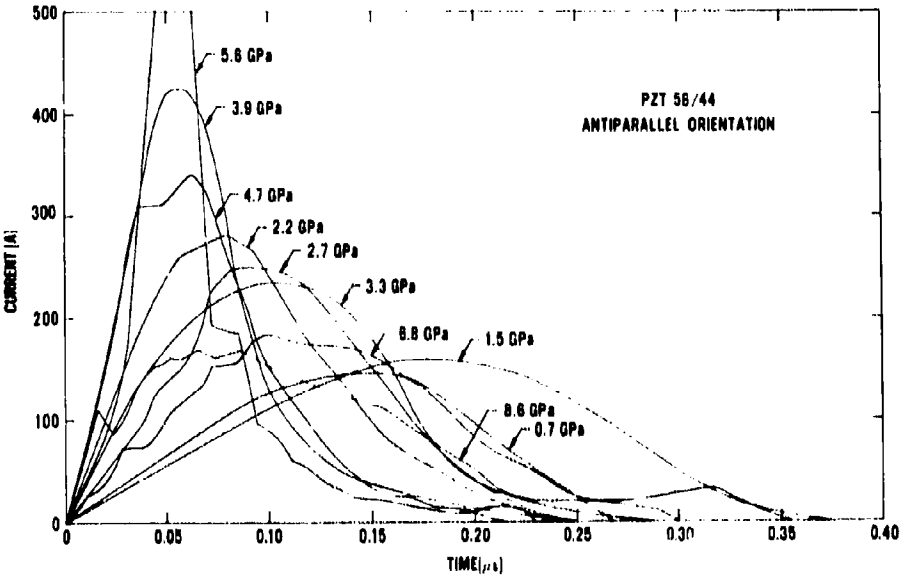

Figure 26. Current pulses for the antiparallel orientation shots.

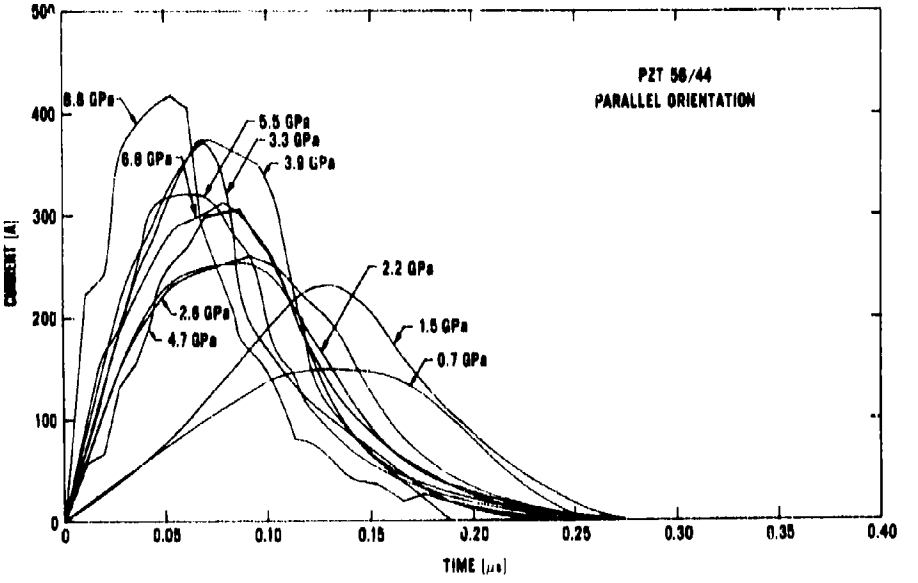

Figure 27. Current pulses for the parallel orientation shots.

Table 5. Results of ultrasonic velocity measurements.

Density (Mg/m^3)	Longitudinal Wave Velocity[a] (km/s)	Shear Wave Velocity[b] (km/s)
7.50	4.56[c]	1.77[d]

[a]Measured for a nominal center frequency of 6 MHz of a broadband pulse.
[b]Measured for a nominal center frequency of 2 MHz of a broadband pulse.
[c]Average of two measurements.
[d]Average of seven measurements.

two-wave shock structure in the PZT disk. The Hugoniot elastic limit of PZT 52/48 material is 1.9 GPa; above this stress, a slower-moving plastic wave is generated in addition to the elastic wave.[12] If it is assumed that the Hugoniot elastic limit of PZT 56/44 is near this value, then a two-wave structure would exist in the shots for stresses of 2.2 GPa or above. The PZT 52/48 plastic wave velocity increases from 1.92 km/s at 2.2 GPa to 2.94 km/s at 8.8 GPa,[12] yielding a plastic wave transit time that decreases from 0.39 to 0.26 μs in this stress range. The strain corresponding to a stress of 8.8 GPa is 0.12. Since the average pulse duration is less than the plastic wave transit times, this suggests that the elastic wave is primarily responsible for the shock depoling of a PZT disk. Figure 15 also indicates this, since the charge release is essentially constant (except for electrical breakdown in Shots 52 and 53) for stresses above about 2.0 GPa, a stress value probably near the Hugoniot elastic limit of PZT 56/44.

Another contribution to the longer-than-expected average pulse duration may be kinetic effects associated with the shock depoling of the PZT 56/44 disks. Lysne and Percival[16] have suggested that kinetic effects should be taken into account to explain the observed current output for the axial-current-mode depoling of PZT 95/5. Lysne and Bartel[17] have developed a kinetic model to explain the response of PZT 65/35 disks subjected to axial-voltage-mode depoling. Kinetic effects were also observed in axial-voltage-mode shock-reverbation experiments for PSZT 70/30-6 disks.[18] (PSZT 70/30-6 refers to $Pb_{0.99}\ Nb_{0.02}\ ((Zr_{0.70}\ Sn_{0.30})_{0.94}Ti_{0.06})_{0.98}O_3$.)

Figure 28 is a comparison of the charge release in the primary depoling current pulses for PZT 56/44, PZT 95/5, and PSZT 68/7. (PSZT 68/7 is a solid solution of 68 mole % lead zirconate, 7 mole % lead titanate, and 25 mole % lead stannate with niobium as a minor added constituent.) The curves for the normally sintered PZT 95/5 and PSZT 68/7 were constructed from a table of values in Reference 3.

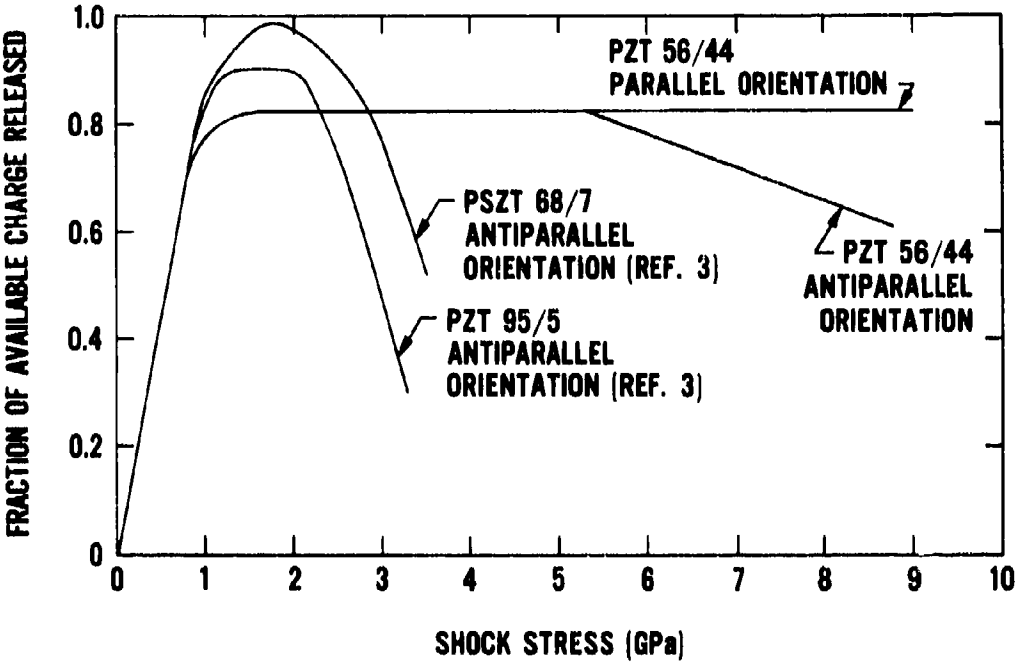

Figure 28. Charge release versus shock stress curves for the axial-current-mode depoling of PZT 56/44, PZT 95/5, and PSZT 68/7 ferroelectric ceramic disks.

The curves for the three materials agree up to a stress of about 1 GPa. In the 1- to 2-GPa stress range, PZT 95/5 and PSZT 68/7 release essentially all the stored charge, but above a stress of about 2 GPa these materials break down electrically.[3,6] In the PZT 56/44 shots for shock stresses above 2 GPa (excluding Shots 52 and 53), it is not known whether incomplete shock depoling or electrical conduction in the PZT material is responsible for the less than complete charge release.

In thirteen of the twenty PZT 56/44 shots, the oscilloscope records indicated a repoling pulse about 1 μs after the initial depoling pulse. These results are given in Table 4. In the majority of observations, only a fraction of the repoling pulse was recorded. A repoling pulse was observed in ten of the eleven shots using quartz impactors. It was probably not observed in Shot 37 because the recording time was too short. The average time from the beginning of the current pulse to the beginning of the repoling pulse for these ten shots is 1.16 μs. The repoling pulses

are probably caused by a decompression of the PZT disk via relief waves starting at the back surface of the impactor or at the 3.45-mm-diameter hole in the brass backup; however, the major relief waves are probably generated at the impactor free surface due to the small size of the hole. The calculated average relief times for the quartz impactor and brass backup are 1.11 μs and 1.09 μs, respectively. These values compare favorably with the 1.16-μs measured time for the repoling pulses. Repoling pulses were observed in two of three shots using PMMA impactors. The average measured time for the pulses was 1.06 μs. Since the relief times for these impactors are about 2 μs, these pulses were probably caused by relief from the hole in the brass backup. A repoling pulse was observed in only one out of six shots using nickel impactors. The measured time of 1.23 μs for the repoling pulse compares favorably with a calculated 1.33-μs relief time for the nickel. The maximum charge recovery for the repoling pulses was measured for the 1.5- and 2.2-GPa antiparallel orientation shots. For these shots, about 15% of the released charge (including both the primary and secondary pulses) was recovered in the repoling pulses. It is estimated that the repoling pulses were recorded for about 80% of their time duration.

Prior to the passage of a shock wave through a short-circuited PZT disk, the bound surface charge neutralizes the polarization charge. The macroscopic electric field inside the ferroelectric is zero. As a shock wave passes through the PZT disk and reduces the remanent polarization vector behind the shock front to a lower value, large induced electric field changes occur. Figure 29 is a schematic depicting the shock depoling of a PZT disk for the antiparallel and parallel orientations, respectively. A single steady shock wave has been assumed. The electric fields E_1 and E_2 are directed away from the shock front for the antiparallel orientation and directed toward the shock front for the parallel orientation.

Since the specimen is short-circuited, the electric fields are related through the Kirchoff equation

$$E_1 Ut = E_2(\ell - Ut), \quad 0 \leq t \leq \tau, \tag{1}$$

where ℓ is the specimen thickness and $\tau = \ell/U$ is the shock transit time. The short circuit current i is related to the electric displacement in Region 2 through the equation

$$i = -A\frac{dD_2}{dt}. \tag{2}$$

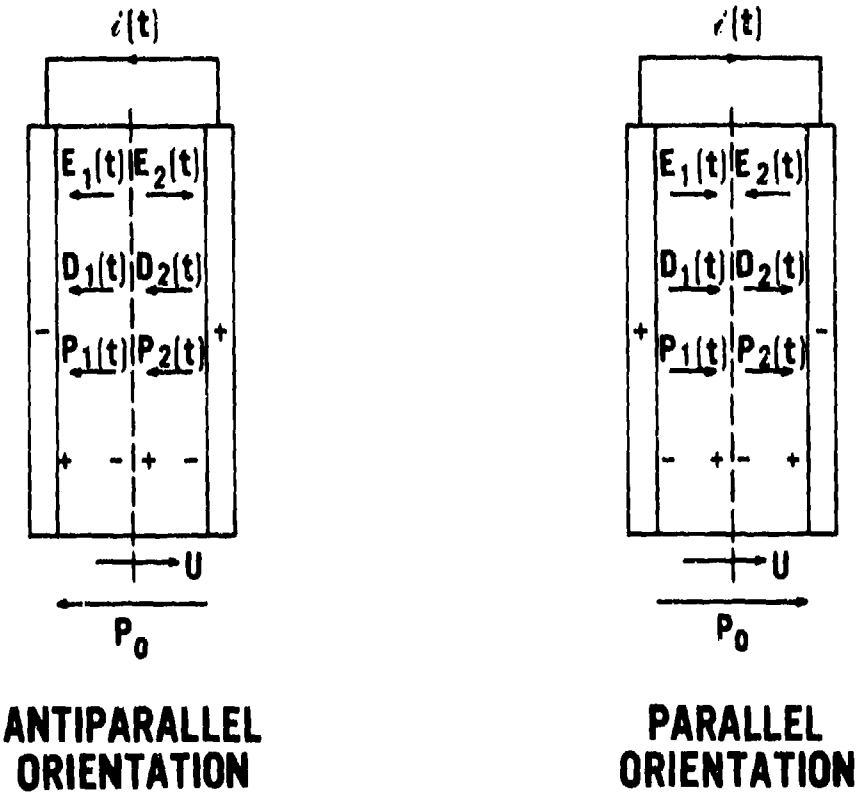

Figure 29. Schematic for the axial-current-mode shock depoling of a PZT disk in the antiparallel and parallel orientations. P_0 is the remanent polarization vector. U is the shock velocity. At time t the shock front is indicated by the dashed line. Regions 1 and 2 are behind and ahead of the shock front, respectively. As the shock wave passes through and depoles the disk, bound surface charge is released. The directions of the electric field E, electric displacement D, and polarization P for the two orientations are shown.

Integrating this equation gives

$$D_2 = P_0 - \int_0^t \frac{i}{A}\, dt . \qquad (3)$$

If it is assumed that no electrical breakdown or conduction occurs in the shocked region of the PZT disk, then the electric displacement vectors in the two regions are equal, thus

$$D_1 = D_2 = D . \tag{4}$$

The case of electrical breakdown and conduction in the shocked region ($D_1 < D_2$) has been treated by Halpin[6] and by Graham and Halpin[5] for the axial-current-mode shock compression of PZT 95/5 and quartz, respectively.

The electric field E_2 for both orientations in Figure 29 is directed opposite to the polarization P_2. To some extent this field can electrically depole the region ahead of the shock wave prior to its eventual shock compression. This field can be estimated from the polarization reversal results in Section III; it will be taken as the field whose initial current slope equals the initial current slope for the shock-depoled PZT disk. Equation (1) is then used to calculate the electric field E_1 behind the shock front.

Behind the shock front, the electric displacement is related to the electric field and polarization through the equation

$$D_1 = \epsilon_0 K_1 E_1 + P_1 , \quad t \geq 0 , \tag{5}$$

where P_1 is the reduced remanent polarization and K_1 is the dielectric constant in the shocked region. Both P_1 and K_1 may be functions of the shock stress σ and the electric field E_1.[2] Two models can be considered for the response of P_1 to shock compression.[16,17,19] In an instantaneous model of shock compression,[19] the initial remanent polarization P_0 is reduced to a constant value P_1 as the shock wave enters the PZT disk and remains at that value. For complete depoling, $P_1 = 0$. In a kinetic model of shock compression,[16,17] P_0 is reduced to a value P_1 as the shock wave enters the disk; P_1 subsequently decays with some time constant to a final value as the shock wave propagates through the disk. One reason that changes in P_1 may lag the shock compression of the disk is that the initially large generated electric field E_1 might cause some repoling of the region behind the shock front.

Figures 30 and 31 give estimates of the electric fields E_1 and E_2, and the electric displacement D for the 2.2-GPa antiparallel orientation shot and the 6.8-GPa parallel orientation shot. For all the shots, the maximum values for the electric fields E_1 and E_2 are estimated to range from about 4 to 24 kV/mm and 1 to 6 kV/mm, respectively, as the shock stress is increased. The 4.56-km/s ultrasonic longitudinal wave velocity was used to calculate the shock transit times in Figures 30 and 31. The electric displacement D is assumed to be continuous in the shocked and unshocked regions and was obtained from Equations (3) and (4). The electric fields E_2 for the 2.2- and 6.8-GPa shots correspond to the polarization reversal current pulses with initial slopes of 5.8 and 6.7 kA/μs, respectively. E_2 increases in a linear manner for about 0.04 to 0.05 μs and then remains constant at the coercive field until shock transit time. The coercive field values for these shots are 4.3 and 4.9 kV/mm, respectively. E_1 decreases in a linear manner for 0.04 to 0.05 μs and then decreases as $(\tau/t) - 1$ until shock transit time. Near t = 0, E_1 has a magnitude of about 17 kV/mm. This value can be compared with the large electric fields of about 10 to 16 kV/mm that were generated in the PZT disks prior to electrical breakdown at about 0.15 to 0.20 μs in the polarization reversal measurements (see Figure 7). Halpin[6] calculated a value for E_1 of about 7 kV/mm near t = 0 using a coercive field value of about 3 kV/mm for a PZT 95/5 disk impacted at 3.4 GPa in the axial current mode. For both of the PZT 56/44 shots, about 6% of the charge release in the primary pulses occurred after the calculated shock transit time. The current pulse durations for the 2.2- and 6.8-GPa shots were 0.24 and 0.27 μs, respectively. After shock transit time, the electric field E_1 in the shock compressed region is zero. If kinetic effects[16-18] associated with polarization change are responsible for the longer-than-expected pulse durations, then the remanent polarization vector in the shocked region decays by about 0.016 $\mu C/mm^2$ after the shock transit time.

Electrical breakdown occurred for the 6.8-GPa antiparallel orientation shot. Since the magnitude of E_1 near t = 0 is about 17 kV/mm for the parallel orientation, this field is expected to have a similar magnitude for the antiparallel orientation shot prior to significant electrical breakdown. Figures 24 and 25 indicate that when electrical breakdown occurs in the PZT disk the released charge in the primary pulse is reduced for about the first half of the pulse duration and then shows recovery for the remainder of the pulse duration. Since in the shocked region the electric field is initially largest and the dielectric strength is presumably reduced, breakdown is expected in this region. This causes less charge flow in the external short circuit and consequently would cause less electrical depoling of the region ahead of the shock front. For later times the breakdown current is reduced, since E_1 decreases with time. The recovery of the primary pulse would then result from the shock depoling of material that was not previously depoled electrically.

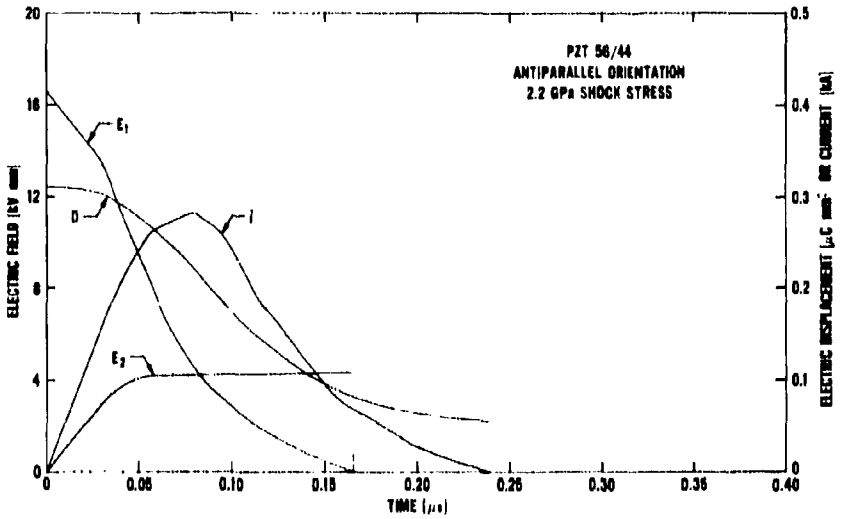

Figure 30. A plot of the current pulse i, the electric fields E_1 and E_2 in the shocked and unshocked regions, respectively, and the electric displacement D in the PZT specimen for the 2.2 GPa antiparallel orientation shot. The 0.17-μs estimated shock transit time is indicated by the dashed line in the figure.

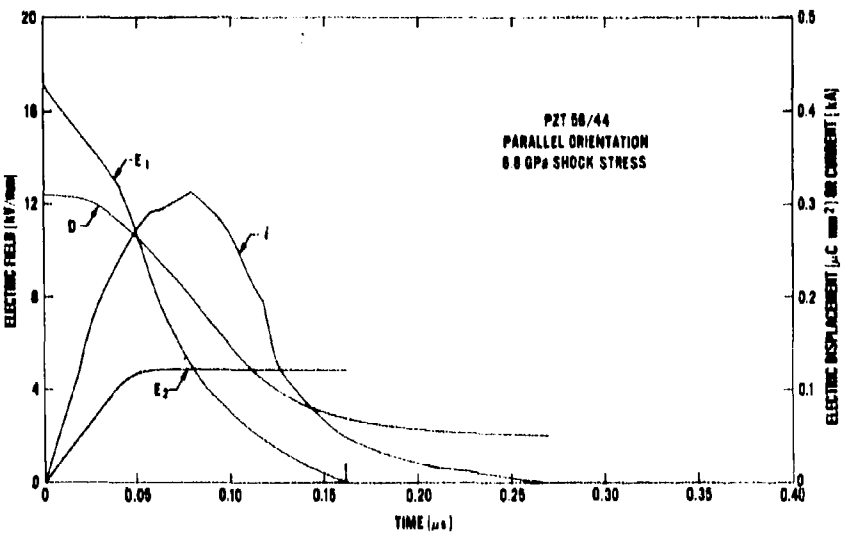

Figure 31. A plot of the current pulse i, the electric fields E_1 and E_2 in the shocked and unshocked regions, respectively, and the electric displacement D in the PZT specimen for the 6.8 GPa parallel orientation shot. The 0.17-μs estimated shock transit time is indicated by the dashed line in the figure.

The current pulses in Figures 30 and 31 have peak values of about 300 A. These peak values are about 50% larger than an average current value of 200 A for each shot that would be obtained if the charge in the primary pulse had been released in a linear manner by the shock wave. For about 30% of the primary pulse duration in each shot the current exceeded the average value. This corresponds to a charge release of about 13% and 16% of the primary pulse for the 2.2- and 6.8-GPa shots, respectively. A linear charge release would occur for the uniform shock depoling of the region behind the shock front and no electrical depoling of the region ahead of the shock front. This suggests that a linear charge release might be obtained for a pyroelectric (a polar material whose dipole moments cannot be reversed in an electric field), but not ferroelectric material. For a pyroelectric material, the region ahead of the shock front may not be electrically depoled prior to shock compression.

The reduction in the outputs for the 6.8- and 8.6-GPa antiparallel orientation shots relative to the parallel orientation shots agrees with the observations of Cutchen.[4] In the axial-mode shock depoling of PZT 65/35 disks, voltage pulses were measured as a function of the risetime of the pressure profiles that were introduced into the material.[4] For the shorter risetimes, the outputs of the antiparallel orientation shots were degraded compared with the parallel orientation shots. Since PZT materials have predominately p-type conductivity at atmospheric pressure,[20] Cutchen, in an extension of the results of Graham[21] for X-cut quartz, proposed that the polarity effects in PZT 65/35 are due to the liberation of positive charge carriers at the shock front, which are then acted upon by the large electric fields in the shocked region. For the parallel orientation, the positive charge carriers are swept from the stressed region and travel with the moving shock front due to the direction of the electric field in the shocked region. For the antiparallel orientation, the charge carriers are accelerated into the stressed region due to the opposite direction of the electric field, thereby causing electrical breakdown and conduction to occur. The stressed region is presumed to have a reduced dielectric strength. The original model of Graham[21] was used by Graham and Halpin[5] to explain the polarity effects in shock-loaded X-cut quartz. For quartz, the charge carriers are presumed to be electrons liberated by stress-induced dislocation motion.

The dielectric constant K_1 in the shocked region near $t = 0$ can be estimated using Equations (1) and (5). Near $t = 0$, $E_2 = \alpha t$ where α is the initial slope of the electric field curve for Region 2. Therefore, $E_1(0) = (\ell/U)\alpha$. Since $D_1(0) = P_0$, we obtain from Equation (5)

$$K_1 = \frac{P_0 - P_1}{\epsilon_0 E_1(0)}. \qquad (6)$$

To obtain α for each shot it is necessary to use the average ratio R for the initial slopes of the electric field and current curves for the polarization reversal measurements in Table 2. This ratio is R = 17(kV mm^{-1}/μs)/(kA/μs). α is then obtained using R and the initial current slopes in Table 4. The value of $P_0 - P_1$ for each shot is taken to be the charge release in the primary depoling current pulse. By doing this, we are assuming an instantaneous model for shock depoling, since Equation (6) applies near t = 0 and the P_1 values used in this equation were obtained at a time corresponding to the pulse duration. Due to kinetic effects, the polarization P_1 near t = 0 may be much different from its value at a later time.[16] Also, there is additional uncertainty in the P_1 value if electrical breakdown or conduction occurs in the PZT material. The calculated dielectric constant K_1 for each shot should therefore be considered only an estimate. Figure 32 shows these estimated dielectric constants versus shock stress. Since the initial electric field $E_1(0)$ varied from about 4 to 24 kV/mm (excluding Shot 57, which was about 60 kV/mm) as the shock stress was increased, K_1 decreased with shock stress because the $P_0 - P_1$ values are essentially independent of stress above about 2 GPa.

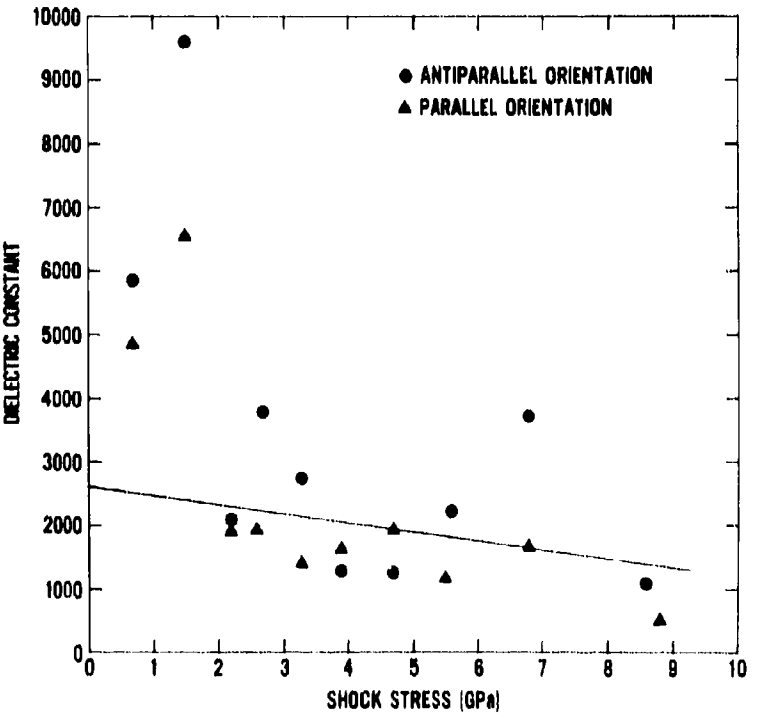

Figure 32. Estimated initial dielectric constant in the shocked region versus shock stress. The straight line is a least-squares fit for the shots with stresses above 2 GPa. The line is extrapolated into the region below 2 GPa.

A linear least-squares fit of the data above 2 GPa gives $K_1 = 2600 - 140\sigma$, where σ is the shock stress in gigapascals. The K_1 values for shock stresses of 0.7 and 1.5 GPa were not included in the least-squares fit since they were much larger than the majority of the values, possibly due to the larger impactor-specimen closure times for the lower projectile velocities. The dielectric constant values in Figure 32 can be compared with the low-frequency dielectric constant of 2480 for unshocked PZT 56/44 listed in Table 1.

Previous investigations of the dielectric constant under shock conditions have been made for other ferroelectric ceramic materials.[6,22,23] In PZT 95/5 axial-current-mode experiments Halpin[6] used a value of 1900 for the dielectric constant behind the shock front in a curve fit to an experimental current-time pulse at 3.4 GPa. Lysne and Percival[22] have recently shown that the dielectric constant of PZT 95/5 decreased from about 2300 to 1000 at a shock stress of 1.4 GPa in normal-voltage-mode experiments. Also, Brody and Wittekindt[23] estimated a dielectric constant of about 2000 behind the shock front in axial-current-mode experiments on barium titanate at a stress of 10 GPa.

VI. SUMMARY

The electrical properties of shock-depoled PZT 56/44 ferroelectric ceramic disks have been investigated in the stress range from 0.7 to 8.8 GPa. External short-circuit current pulses were measured as the shock wave propagated axially through the disk in a direction either parallel or antiparallel to the material remanent polarization vector. As the shock stress was increased, the peak current increased and shifted to earlier times. Complete charge release was not observed in any of the shots. The charge release for the two orientations agreed up to a stress of about 5.6 GPa. In the stress range from 1.5 to 5.6 GPa, the charge release was essentially constant. About 82% of the available charge was released. At stress levels of 6.8 and 8.6 GPa, degradation effects occurred for the antiparallel orientation shots. For these shots, the charge release was reduced by 14% and 25%, respectively, compared with the parallel orientation shots. In addition to the shock wave measurements, a family of current and voltage pulses was obtained under nonshock conditions to determine the electric field and electrical depoling path for the material ahead of the shock front. The estimated coercive field for this region increased from about 1 to 6 kV/mm as the shock stress was increased. The magnitude of the electric field behind the shock front was also estimated. The initial values for this field increased from about 4 to 24 kV/mm as the shock stress was increased.

REFERENCES

1. B. Jaffe, W. R. Cook, Jr., and H. Jaffe, ***Piezoelectric Ceramics***, Academic Press, NY (1971).

2. P. C. Lysne, "Shock Induced Polarization of a Ferroelectric Ceramic," ***Journal of Applied Physics***, Vol. 48, p. 1024 (1977).

3. W. J. Halpin, "Current for a Shock-Loaded Short-Circuited Ferroelectric Ceramic Disk," ***Journal of Applied Physics***, Vol. 37, p. 153 (1966).

4. J. T. Cutchen, "Polarity Effects and Charge Liberation in Lead Zirconate Titanate Ceramics Under High Dynamic Loads," ***Journal of Applied Physics***, Vol. 37, p. 4745 (1966).

5. R. A. Graham and W. J. Halpin, "Dielectric Breakdown and Recovery of X-Cut Quartz Under Shock-Wave Compression," ***Journal of Applied Physics***, Vol. 39, p. 5077 (1968).

6. W. J. Halpin, "Resistivity Estimates for Some Shocked Ferroelectrics," ***Journal of Applied Physics***, Vol. 39, p. 3821 (1968).

7. D. Berlincourt and H. Krueger, "Domain Processes in Lead Titanate Zirconate and Barium Titanate Ceramics," ***Journal of Applied Physics***, Vol. 30, p. 1804 (1959).

8. W. A. Wooster and A. Breton, ***Experimental Crystal Physics***, Clarendon Press, Oxford (1970).

9. R. H. Plumlee, ***High Field Polarization Reversal in Polycrystalline Ferroelectrics***, SC-RR-69-391, Sandia Laboratories, Albuquerque, NM (October 1969).

10. R. H. Plumlee, ***Ferroelectric Switching Time Measurements***, SLA-73-0212, Sandia Laboratories, Albuquerque, NM (February 1973).

11. W. Mock, Jr. and W. H. Holt, ***The NSWC Gas Gun Facility for Shock Effects in Materials***, NSWC/DL TR-3473, Naval Surface Weapons Center, Dahlgren, VA (July 1976).

12. C. E. Reynolds and G. E. Seay, "Two-Wave Shock Structures in the Ferroelectric Ceramics Barium Titanate and Lead Zirconate Titanate," ***Journal of Applied Physics***, Vol. 33, p. 2234 (1962).

13. W. J. Halpin and R. A. Graham, "Shock Wave Compression of Plexiglas from 3 to 20 Kilobars," ***Proceedings of Fourth Symposium (International) on Detonation***, ACR-126, U. S. Government Printing Office, Washington, DC, p. 222 (1965).

14. R. A. Graham, "Piezoelectric Current from Shunted and Shorted Guard Ring Quartz Gauges," ***Journal of Applied Physics***, Vol. 46, p. 190 (1975).

15. Los Alamos Scientific Laboratory, ***Selected Hugoniots***, LA-4167-MS, prepared by Group GMX-6, Los Alamos, NM.

16. P. C. Lysne and C. M. Percival, "Analysis of Shock-Wave-Activated Power Supplies," ***Ferroelectrics***, Vol. 10, p. 129 (1976).

17. P. C. Lysne and L. C. Bartel, "Electromechanical Response of PZT 65/35 Subjected to Axial Shock Loading," ***Journal of Applied Physics***, Vol. 46, p. 222 (1975).

18. P. C. Lysne, "Kinetic Effects in the Electrical Response of a Shock-Compressed Ferroelectric Ceramic," ***Journal of Applied Physics***, Vol. 46, p. 4078 (1975).

19. P. C. Lysne, "Dielectric Breakdown of Shock-Loaded PZT 65/35," ***Journal of Applied Physics***, Vol. 44, p. 577 (1973).

20. R. Gerson and H. Jaffe, "Electrical Conductivity in Lead Titanate Zirconate Ceramics," ***Journal of Physics and Chemistry of Solids***, Vol. 24, p. 979 (1963).

21. R. A. Graham, "Dielectric Anomaly in Quartz for High Transient Stress and Field," ***Journal of Applied Physics***, Vol. 33, p. 1755 (1962).

22. P. C. Lysne and C. M. Percival, "Electric Energy Generation by Shock Compression of Ferroelectric Ceramics: Normal-Mode Response of PZT 95/5," ***Journal of Applied Physics***, Vol. 46, p. 1519 (1975).

23. P. S. Brody and R. H. Wittekindt, ***Dielectric Constant of Barium Titanate at 100 Kilobars***, TR-917, Diamond Ordnance Fuse Laboratories, Washington, DC (March 1961).

APPENDIX A

OSCILLOSCOPE RECORDS FOR POLARIZATION REVERSAL EXPERIMENTS

(a) (b)

Figure A-1. Polarization-reversal voltage and current records for a PZT disk for a source capacitor voltage of 2 kV. (a) Voltage record. The vertical scale is 1 kV/div and the horizontal scale is 0.1 μs/div. (b) Current record. The vertical scale is 143 A/div and the horizontal scale is 0.1 μs/div.

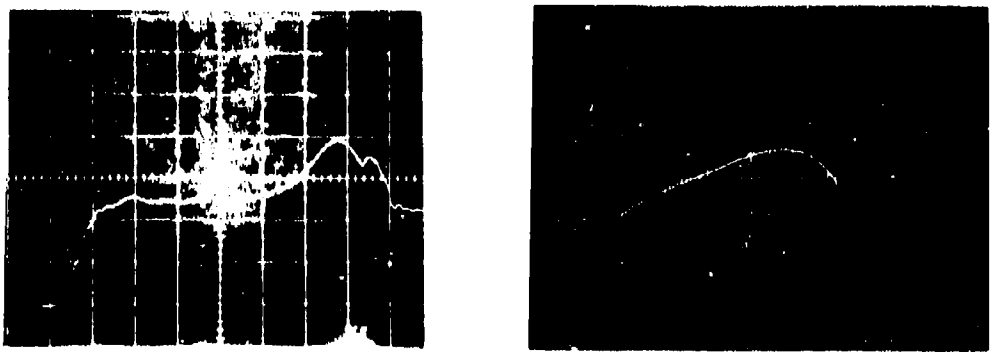

(a) (b)

Figure A-2. Polarization-reversal voltage and current records for a PZT disk for a source capacitor voltage of 3 kV. (a) Voltage record. The vertical scale is 1 kV/div and the horizontal scale is 0.05 μs/div. (b) Current record. The vertical scale is 143 A/div and the horizontal scale is 0.05 μs/div.

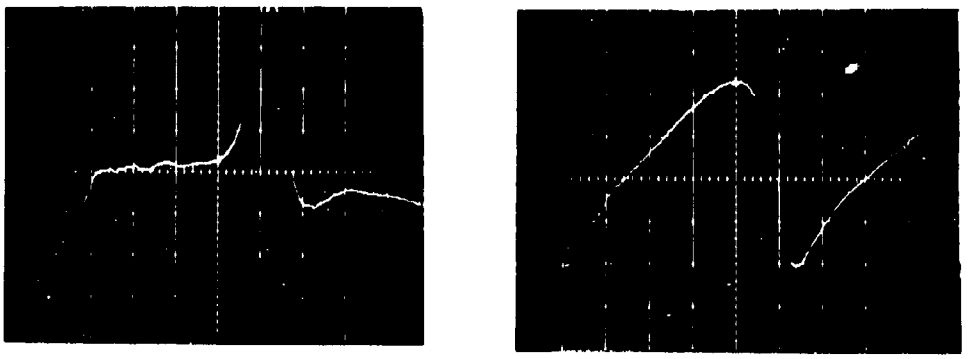

(a) (b)

Figure A-3. Polarization-reversal voltage and current records for a PZT disk for a source capacitor voltage of 4 kV. (a) Voltage record. The vertical scale is 1 kV/div and the horizontal scale is 0.05 μs/div. (b) Current record. The vertical scale is 143 A/div and the horizontal scale is 0.05 μs/div.

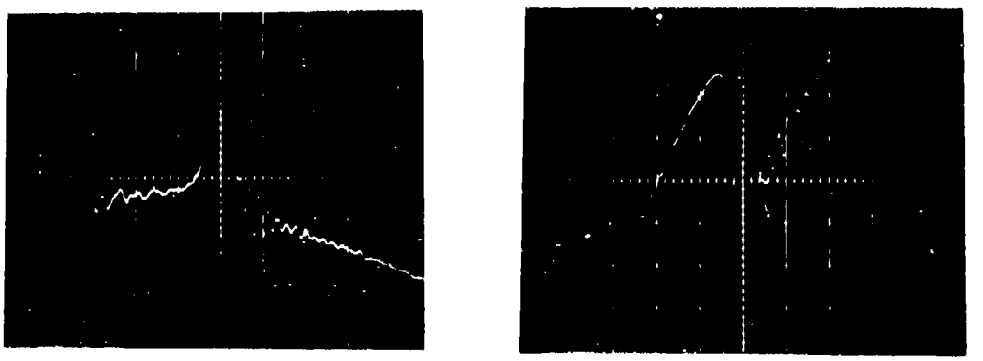

(a) (b)

Figure A-4. Polarization-reversal voltage and current records for a PZT disk for a source capacitor voltage of 6 kV. (a) Voltage record. The vertical scale is 1 kV/div and the horizontal scale is 0.05 μs/div. (b) Current record. The vertical scale is 143 A/div and the horizontal scale is 0.05 μs/div.

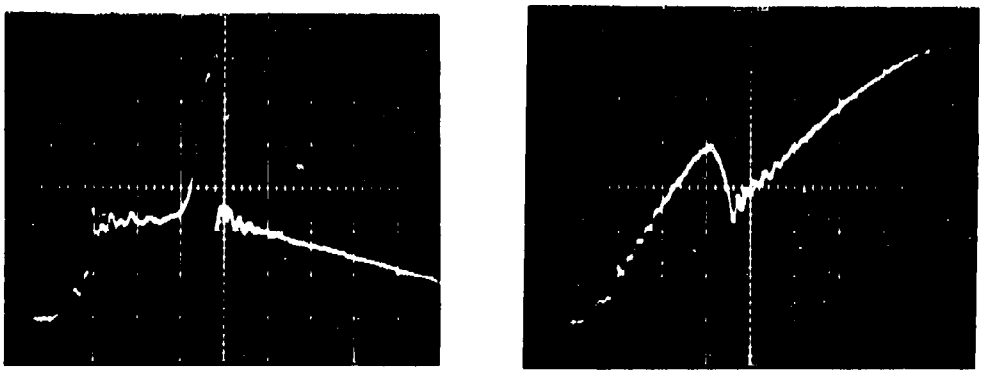

(a) (b)

Figure A-5. Polarization-reversal voltage and current records for a PZT disk for a source capacitor voltage of 7 kV. (a) Voltage record. The vertical scale is 2 kV/div and the horizontal scale is 0.05 μs/div. (b) Current record. The vertical scale is 286 A/div and the horizontal scale is 0.05 μs/div.

APPENDIX B

OSCILLOSCOPE RECORDS FOR SHOCK-DEPOLING EXPERIMENTS

(Each figure shows the record for the antiparallel orientation shot on the left and the record for the parallel orientation shot on the right for the corresponding shock stress. The shock stress increases with increasing figure number. Time increases from left to right in the figures unless otherwise noted.)

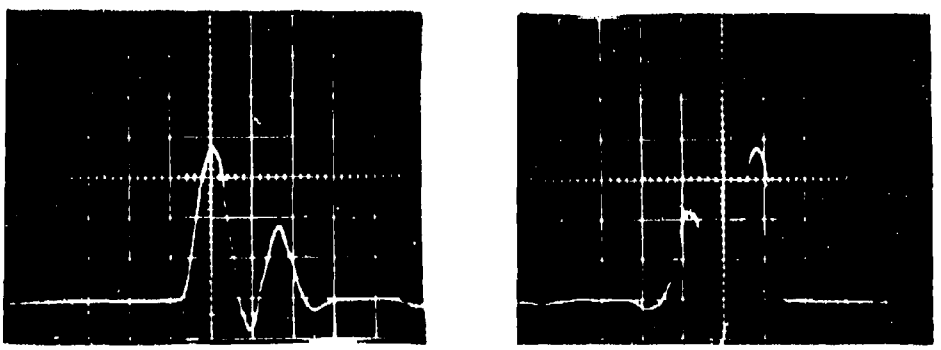

(a) (b)

Figure B-1. Current records for (a) Shot 38 and (b) Shot 39. In (b) time increases from right to left. The vertical scale is 40 A/div and the horizontal scale is 0.2 μs/div.

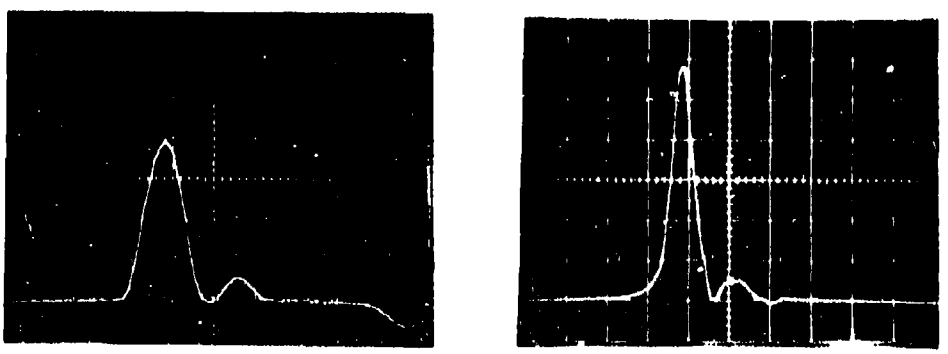

(a) (b)

Figure B-2. Current records for (a) Shot 42 and (b) Shot 41. The vertical scale is 40 A/div and the horizontal scale is 0.2 μs/div.

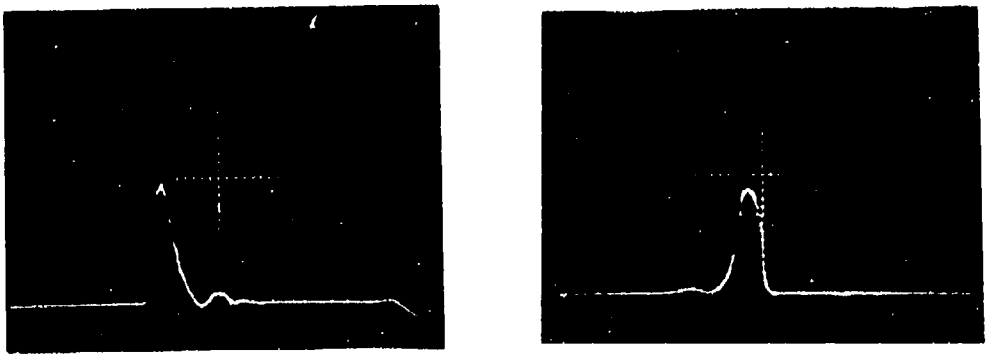

(a) (b)

Figure B-3. Current records for (a) Shot 36 and (b) Shot 37. In (b) time increases from right to left. The vertical scale is 100 A/div and the horizontal scale is 0.2 μs/div.

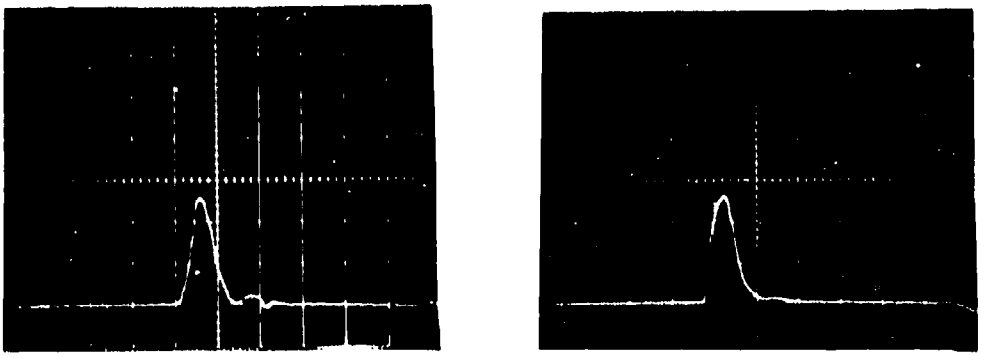

(a) (b)

Figure B-4. Current records for (a) Shot 49 and (b) Shot 45. The vertical scale is 100 A/div and the horizontal scale is 0.2 μs/div.

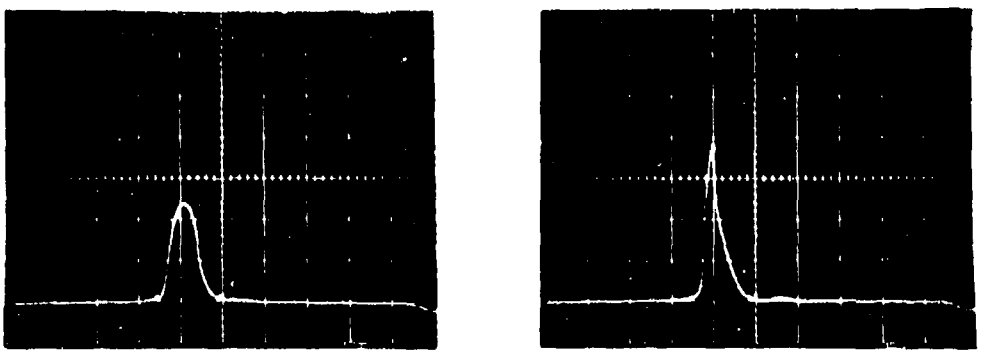

(a) (b)

Figure B-5. Current records for (a) Shot 44 and (b) Shot 46. The vertical scale is 100 A/div and the horizontal scale is 0.2 μs/div.

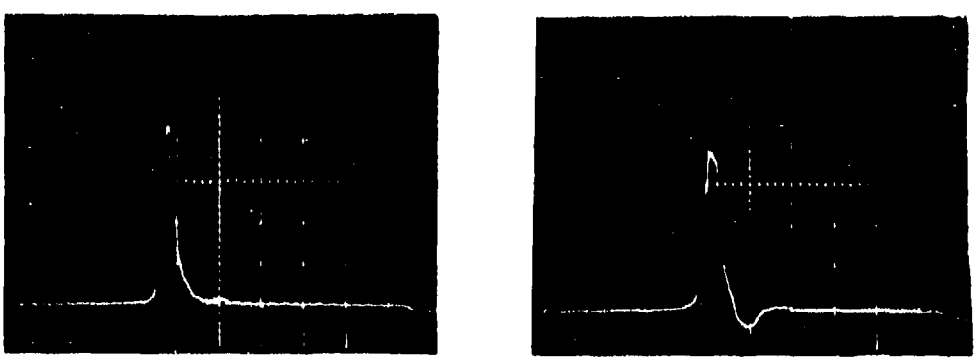

(a) (b)

Figure B-6. Current records for (a) Shot 48 and (b) Shot 47. The vertical scale is 100 A/div and the horizontal scale is 0.2 μs/div.

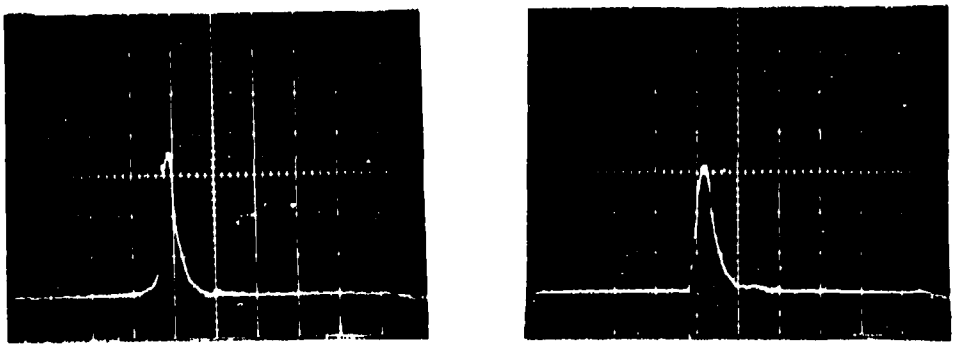

(a) (b)

Figure B-7. Current records for (a) Shot 50 and (b) Shot 51. The vertical scale is 100 A/div and the horizontal scale is 0.2 μs/div.

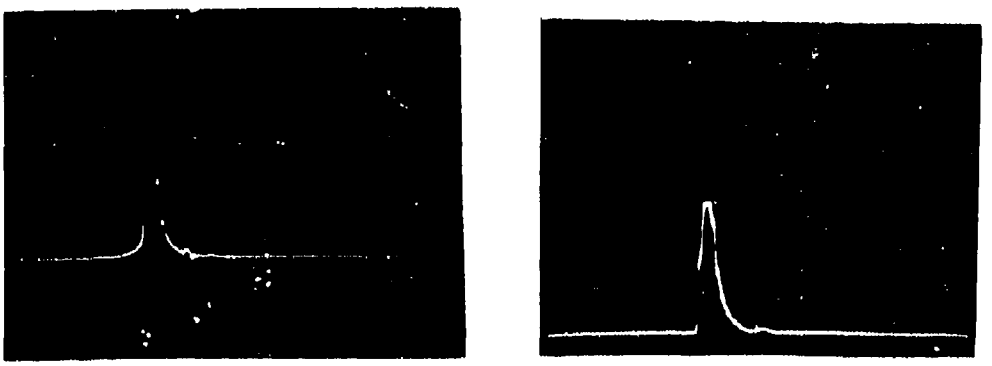

(a) (b)

Figure B-8. Current records for (a) Shot 54 and (b) Shot 55. The vertical scale is 100 A/div and the horizontal scale is 0.2 μs/div.

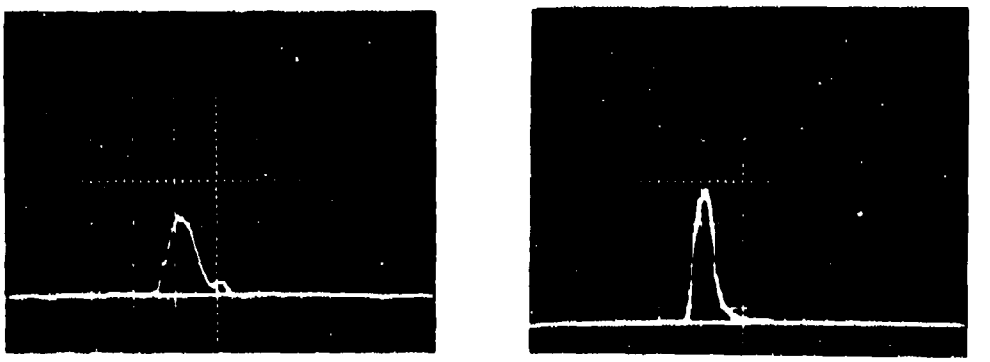

(a) (b)

Figure B-9. Current records for (a) Shot 52 and (b) Shot 56. The vertical scale is 100 A/div and the horizontal scale is 0.2 μs/div.

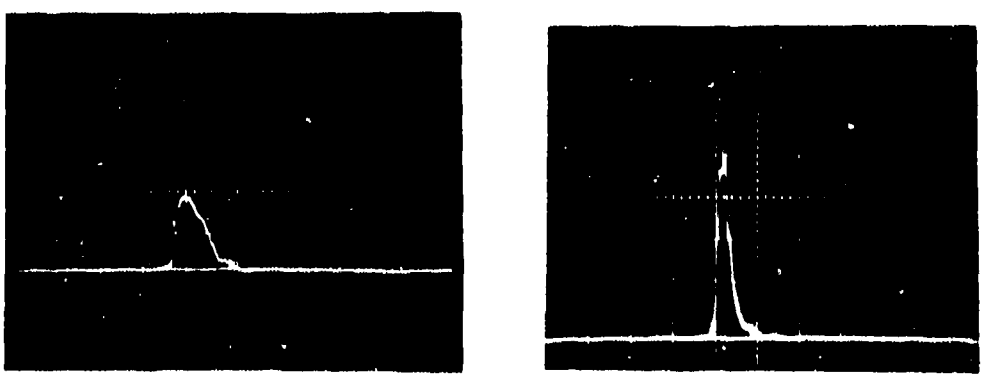

(a) (b)

Figure B-10. Current records for (a) Shot 53 and (b) Shot 57. The vertical scale is 100 A/div and the horizontal scale is 0.2 μs/div.

DISTRIBUTION

Commander
Naval Sea Systems Command
Washington, DC 20360
ATTN: SEA-03B S. R. Marcus
SEA-0331 S. J. Matesky
SEA-0332 W. W. Blaine
SEA-0332 R. A. Bailey
SEA-035 G. N. Sorkin
SEA-0352 M. A. Kinna
SEA-65313C L. H. Hawver

Commander
Naval Air Systems Command
Washington, DC 20360
ATTN: AIR-310A H. J. Mueller
AIR-310B J. W. Willis
AIR-320A T. F. Kearns
AIR-350 E. M. Fisher
AIR-350D H. B. Benefiel
AIR-5324 S. Englander

Office of Naval Research
Department of the Navy
Washington, DC 20360
ATTN: ONR-420 T. G. Berlincourt
ONR-465 E. I. Salkovitz

Office of Naval Research
536 S. Clark St.
Chicago, IL 60605
ATTN: George Sandoz

Commander
Naval Research Laboratory
Washington, DC 20375
ATTN: 6370 S. C. Sanday
6434 E. Skelton
7740 R. K. Parker
7908 W. Atkins
7908 A. Williams

Commander
Naval Weapons Center
China Lake, CA 93555
ATTN: M. E. Backman
S. A. Finnegan
J. Pearson
E. B. Royce

Superintendent
U. S. Naval Academy
Annapolis, MD 21402
ATTN: J. Fontanella

Director
Army Ballistics Research Laboratories
Terminal Ballistics Laboratory
Aberdeen Proving Ground, MD 20015
ATTN: W. S. deRosset
R. E. Franz
G. E. Hauver
G. Moss
R. Vitali

Commander
Army Materials and Mechanics Research Center
Watertown, MA 92172
ATTN: D. T. Dandekar
R. M. Lamothe
J. F. Mescall
P. V. Riffin

Commander
Army Research and Development Command
Dover, NJ 07801
ATTN: C. Christoe
C. deFranco
P. Harris
F. J. Owens

Commander
Harry Diamond Laboratory
Washington, DC 20438
ATTN: P. S. Brody

Los Alamos Scientific Laboratory
Los Alamos, NM 87544
ATTN: J. J. Dick
C. M. Fowler
J. M. Holt, Jr.
J. W. Hopson
J. N. Johnson
R. Morales
J. Morgan
B. W. Olinger
J. Wackerle
Technical Library (2)

Sandia Laboratories
Albuquerque, NM 87115
ATTN: L. C. Bartel
B. M. Butcher
L. W. Davison
J. Gover
R. A. Graham
D. B. Hayes
R. J. Lawrence
P. C. Lysne
C. B. McCampbell
S. Montgomery
D. E. Munson
C. M. Percival
P. M. Richards
G. A. Samara

Lawrence Livermore Laboratory
University of California
Livermore, CA 94550
ATTN: D. L. Banner
S. Cochran
W. H. Gust
E. Nidick, Jr.
H. C. Rodean
J. Shaner

Shock Dynamics Laboratory
Washington State University
Pullman, WA 99163
ATTN: G. E. Duvall
G. R. Fowles

National Bureau of Standards
Washington, DC 20234
ATTN: R. A. MacDonald
D. H. Tsai

Seismological Laboratory
California Institute of Technology
Pasadena, CA 91125
ATTN: T. J. Ahrens

Stanford Research Institute
Poulter Laboratory
333 Ravenswood Avenue
Menlo Park, CA 94025
ATTN: D. Curran
D. C. Erlich
Y. Gupta
L. Seaman
D. Shockey

Defense Documentation Center
Cameron Station
Alexandria, VA 22314 (12)

Library of Congress
Washington, DC 20540
ATTN: Gift and Exchange Division (4)

Local:

C
D
E41
F
F10
F12

F12 (Luessen)
F12 (Berger)
G
G10
G13
G20
G30
G301
G31
G32
G33
G34
G35
G35 (Mock)
G35 (Holt)
G35 (Wishard)
G40
G50
G53
G531
G54
G60
R
R04
R10
R10 (Jacobs)
R11
R13
R13 (Coleburn)
R13 (Erkman)
R13 (Forbes)
R13 (Roslund)
R30
R31
R31 (Augl)
R32
R33
R34
X21